Effects of Turbulence Intensity and Variability on Biodynamic Feedthrough Modeling in Touchscreen Dragging Tasks

Leto, G.; Pool, D.M.

DOI
10.2514/6.2025-0976

Publication date
2025

Document Version
Final published version

Published in
Proceedings of the AIAA SCITECH 2025 Forum

AIAA SciTech Forum
6-10 January 2025, Orlando, FL
AIAA SCITECH 2025 Forum

10.2514/6.2025-0976

Effects of Turbulence Intensity and Variability on Biodynamic Feedthrough Modeling in Touchscreen Dragging Tasks

Giulia Leto* and Daan M. Pool†
Delft University of Technology, Delft, Zuid-Holland, The Netherlands

Recent aircraft have seen the implementation of touchscreens (TSCs) on the flight deck, as they enable more intuitive and direct human-machine interactions. However, biodynamic feedthrough (BDFT), i.e., the direct transmission of the aircraft's accelerations through the pilot's body to the control inputs, is a cause for concern, preventing safe and reliable use of TSCs in turbulence. This paper describes a simulator experiment evaluating the performance of model-based mitigation of BDFT in a TSC dragging task performed in turbulence. In the experiment, a total of nine different vertical (heave) motion perturbations were tested: multisine signals resembling turbulence, stationary (Gaussian) and variable (patchy) simulated turbulence, each at three intensity levels (RMS acceleration of 0.75, 0.5, and 0.25 m/s^2). For the multisine turbulence signals, on average over 87% accuracy of the identified personalized BDFT models was achieved for the high and medium turbulence levels, reducing to 74% for the low-intensity turbulence due to degraded BDFT consistency. Furthermore, BDFT models fitted to the Gaussian turbulence data were found to achieve an accuracy comparable to that observed for the multisine motion disturbances, with only 3.5% lower performance on average. As expected, for the more time-varying patchy turbulence cases, model-based BDFT cancellation was found to be 4.7% lower than for the Gaussian turbulence data. Finally, models generalizing BDFT dynamics across participants or experimental runs were found to always be outperformed by individual participant and individual trial models, giving up to 10% higher identification performance. Overall, these findings show that a model-based approach to canceling the effects of BDFT mitigation for TSCs in turbulence is promising, but that real-time identification and time-varying BDFT models will be needed to achieve consistently high mitigation performance in realistic variable turbulence.

Nomenclature

Abbreviations

BDFT	=	Biodynamic Feedthrough	P	=	Patchy condition
CW	=	Classical Washout filter	PDF	=	Probability Density Function
FRF	=	Frequency Response Function	PSD	=	Power Spectral Density
G	=	Gaussian condition	RMS	=	Root-Mean-Square
IR	=	Individual-Run	SA	=	Subject-Averaged
M	=	Multisine condition	SNR	=	Signal-to-Noise Ratio
NM	=	No Motion	SRS	=	SIMONA Research Simulator
OSFA	=	One-Size-Fits-All	TSC	=	Touchscreen

Symbols

A	=	Sinusoid amplitude	u	=	TSC input signal
CF	=	Crest Factor	u^{BDFT}	=	BDFT component of the TSC input
CI	=	Cancellation Index	$\hat{u}^{BDFT}$	=	Modeled BDFT component of the TSC input
e	=	Error signal	u^{CANC}	=	Canceled TSC input signal
f	=	Position forcing function	u^{COG}	=	Cognitive component of the TSC input
f''	=	Acceleration forcing function	V	=	Velocity

*Ph.D. student, Control and Operations department, Faculty of Aerospace Engineering, P.O. Box 5058, 2600GB Delft, The Netherlands; g.leto@tudelft.nl.
†Assistant Professor, Control and Simulation section, Faculty of Aerospace Engineering, P.O. Box 5058, 2600GB Delft, The Netherlands; d.m.pool@tudelft.nl. Associate Fellow AIAA.

G_{BDFT}	=	Gain of the BDFT model	VAF	=	Variance Accounted For
H_{BDFT}	=	BDFT model	V_{metric}	=	Intensity metric
$\hat{H}_{BDFT}$	=	BDFT model estimates	$\ddot{x}$	=	Surge accelerations
J	=	Cost function	$\ddot{y}$	=	Sway accelerations
K	=	Kurtosis	$\ddot{z}$	=	Heave accelerations
K_{heave}	=	Gain of CW16 filter	δ	=	BDFT model parameter array
L_{u_g}	=	Turbulence length scale	ζ_{BDFT}	=	Damping ratio of the BDFT model
N	=	Number of points	μ	=	Mean
n	=	Remnant	ρ_u^2	=	Relative remnant
n_{ty}, n_{tz}, n_d	=	Integer factors of the sinusoid frequency	σ	=	Standard Deviation
Q	=	Kurtosis related parameter	σ_g^2	=	Turbulence intensity
R	=	Patch length parameter	τ_{BDFT}	=	Time delay of the BDFT model
RV	=	Run variability	ϕ	=	Sinusoid phase
$\tilde{S}$	=	Estimated PSD	ω	=	Sinusoid frequency
S	=	PSD	ω_{BDFT}	=	Break frequency of the BDFT model
t	=	Time	ω_{heave}	=	Gain of CW16 filter
T_m	=	Measurement time	ω_m	=	Base frequency
Subscripts					
d	=	Disturbance	y	=	Horizontal component
i, j, k	=	Indices	z	=	Vertical/heave component
t	=	Target			

I. Introduction

Touchscreens see increasingly more use in aircraft cockpits as a crucial input device for interacting with critical aircraft and autopilot systems [1–5], mainly thanks to their capacity as a direct manipulation interface. However, a number of important issues still need to be addressed before TSCs can be effectively used for safety critical tasks, especially in dynamic environments such as an aircraft cockpit in turbulence. Providing an input on a TSC requires pilots to precisely touch the screen in the location of a (virtual) button, move along a slider, or perform some other very specific gesture. Such straightforward actions are known to quickly become difficult when performed in the presence of vehicle accelerations or vibrations, especially with an interface that lacks tactile feedback [6, 7]. The propagation of vehicle accelerations to perturbed movements of pilots' fingers, a phenomenon called biodynamic feedthrough (BDFT) [8], will directly cause involuntary touches to be registered as control inputs.

A significant number of prior studies have focused on potential strategies for TSC BDFT mitigation [3, 6, 9–15]. For example, BDFT-induced error rates were found to be higher with projected capacitive TSCs compared to resistive touch technologies, and will also worsen with decreasing screen size [3]. Also the TSC location affects BDFT susceptibility: testing TSC positions overhead, in front, inboard and outboard of the pilot showed that the frontal position results in the lowest error rates, while an inboard location causes the least fatigue [3, 6, 14, 16, 17]. The use of interchangeable stencil overlays was proposed to separate the input areas for discrete interaction with TSCs and mitigate BDFT effects [10, 18], but was found to have limited impact and also to somewhat compromise the flexibility of the TSC interfaces. Similarly, TSCs equipped with additional grips at the edges of the display or additional wrist or arm supports were also found to be constraining and, an in most cases, ineffective in reducing error rates [12]. A promising support of this kind is 'braced touch', a configuration in which users support their hands directly on the display, which proved to be effective for mitigating BDFT effects in combination with a double tap activation method [11].

The most promising BDFT mitigation strategy for TSCs, however, does not attempt to physically mitigate BDFT as in the works discussed in the previous paragraph. A *model-based BDFT mitigation* approach, where BDFT-induced finger movements are predicted using human biodynamic models and (measured) vehicle accelerations, has been shown to enable software-based cancellation of more than 70% of involuntary BDFT-induced finger movements [13–15]. Although promising, this mitigation approach has only been tested on the BDFT data recorded in flight simulator experiments with multisine motion disturbance signals, loosely mimicking the accelerations of an aircraft in turbulence [13, 14]. The effectiveness of this model-based BDFT cancellation approach in real turbulent flight conditions has therefore yet to be quantified, as in reality vehicle motion perturbations will have a broader and continuous frequency spectrum. Furthermore, the methods and models that have so far been used for the identification of BDFT models assume linear time-invariant BDFT dynamics, which may not be permissible for actual turbulence, which is inherently

variable and patchy in nature. Finally, the approach has been proven able to reliably identify a model for the BDFT component of the input when the occurring BDFT is sufficiently strong [14]. Because the reliability of BDFT models is crucial for the successful cancellation of BDFT, understanding the effect of motion intensity on the human BDFT dynamics and modeling them is essential for successful implementation of model-based cancellation in TSCs in aircraft cockpits.

The goal of this paper is therefore to evaluate the use of model-based mitigation of BDFT in turbulent conditions in continuous TSC dragging tasks, focusing on the effects of turbulence signal variability and intensity. New human-subject data were collected using an experiment with the SIMONA Research Simulator at TU Delft, in which 21 volunteers were asked to track a target on a TSC placed directly in front of them, while exposed to motion disturbances in the heave axis. For simulated motion perturbations, a multisine signal mimicking turbulence and two simulated turbulence signals (Gaussian and Patchy) obtained from a nonlinear Cessna Citation II simulation model were compared, all three for three intensity levels (low, medium, high). The parameters for a time-invariant BDFT model were identified from both the multisine and the stationary (Gaussian) turbulence motion disturbances using a time-domain fitting algorithm [19]. These BDFT models were tested for their effectiveness for canceling the BDFT at all motion intensity levels and with the time-varying (Patchy) turbulence, to verify the extent to which TSC users may adapt their neuromuscular (and hence BDFT) dynamics to changes in the experienced motion perturbations.

The structure of this paper is as follows: Section II.A introduces the method of model-based BDFT mitigation and the issues related to modeling BDFT in (simulated) realistic turbulence, as opposed to multisine motion disturbances. The experimental set-up and experiment design are discussed in Section III, together with the hypotheses for the research. The results of the experiment are presented in Section IV and subsequently discussed in Section V. Finally, the main conclusions are drawn in Section VI.

II. Model-Based Biodynamic Feedthrough Cancellation

A. Biodynamic Feedthrough Cancellation Framework

Fig. 1 schematically shows the working principle of model-based BDFT cancellation for a human controller who is performing a TSC dragging task in turbulent flight. Furthermore, the main variables that potentially affect BDFT occurrence and dynamics that are studied in this paper are indicated in this figure. The human controller is exposed to an acceleration signal f_d'' (motion disturbance) while tracking a target with position f_t on a TSC. In this task, following the well-known quasi-linear human operator models for manual control tasks [20, 21], the human controller is assumed to have quasi-linear dynamics: the position of the finger of the operator, i.e., the input u given to the TSC is the superposition of a cognitive voluntary component u^{COG}, linearly related to the control task f_t, an involuntary BDFT component caused by the transfer of the vehicle's accelerations f_d'' through the body and limbs of the human, and a remnant n accounting for nonlinearities [13, 14]:

$$u = u^{BDFT} + u^{COG} + n \tag{1}$$

Fig. 1 further shows how a BDFT model $H_{BDFT}(s)$ – i.e., a transfer function model that maps the vehicle's accelerations to the resulting involuntary input on the TSC – may be used to predict the involuntary component u^{BDFT}, and how a canceled input signal u^{CANC} can be calculated. This canceled input signal may then be used as an estimate of the original voluntary component of the input u^{COG}, see Eq. (2) and the blue block of Fig. 1:

$$u^{CANC} = u - \hat{u}^{BDFT} \tag{2}$$

Naturally, the accuracy of the BDFT model $H_{BDFT}(s)$ is essential for achieving effective model-based mitigation of the occurring BDFT. To accurately identify BDFT models, however, both the control task and the motion disturbance have to be designed specifically for the purpose of identification, inevitably affecting the dynamics that are identified. In fact, to be able to separate the involuntary component of the input registered by a TSC from voluntary component and remnant, and to relate the BDFT component of the input to the accelerations at which the human operator is exposed, the disturbance and the target forcing functions need to have discrete contributions to the frequency spectrum that can be explicitly isolated, such as multisine signals [14]. Identification of BDFT occurring under realistic turbulence – which generally has a continuous spectrum and power at all frequencies – is impeded by the impossibility of separating the BDFT components of the input from the remnant. On top of this inherent issue in BDFT modeling in turbulence, differences in spectral distribution, intensity, and intensity variations over time that may occur in realistic turbulence

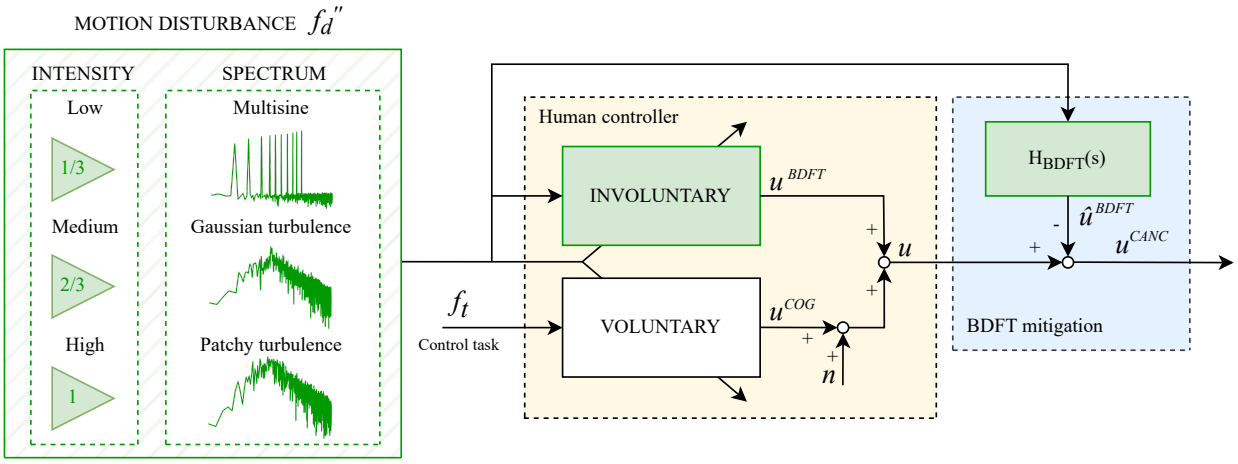

Fig. 1 Quasi-linear human controller dynamics and model-based BDFT mitigation dynamics. The arrow crossing the involuntary and voluntary blocks of the human controller indicate that these dynamics are assumed to adapt when changes in the motion disturbance occur. A graphical representation of the motion disturbances used in the experiment described in this paper is given on the left.

also likely influence how model-based BDFT mitigation will perform. Human controllers most likely adapt their neuromuscular dynamics to maintain good tracking performance when exposed to turbulence with different or varying characteristics; this will also change, as a result, their BDFT dynamics. These potential adaptations are indicated in Fig. 1 with arrows crossing the voluntary and involuntary dynamics blocks.

Finally, as TSC inputs generally require 2-D finger movements on the screen surface, the control input u and the target signal f_t need to be decomposed into a lateral component y and a vertical/longitudinal component z (depending on the orientation of the TSC). This means that the schematic in Fig. 1 describes the contributions to each of these components independently, and can be applied to both [13, 14].

B. Biodynamic Feedthrough Model

Previous research on BDFT occurring with TSCs showed that the lumped BDFT dynamics occurring with a multisine motion disturbance can be captured effectively using the model in Eq. (3). This model consists of three components: an underdamped second-order system encompassing the neuromuscular dynamics, a gain G_{BDFT} capturing the magnitude of the occurring BDFT, and a time delay τ_{BDFT} accounting for the latency in the TSC processing systems [13, 22].

$$H_{BDFT}(s) = G_{BDFT} \cdot \frac{\omega_{BDFT}^2}{s^2 + 2\zeta_{BDFT}\omega_{BDFT} \cdot s + \omega_{BDFT}^2} e^{-s\tau_{BDFT}} \tag{3}$$

Analysis of preliminary data of the current experiment, however, revealed that the measured BDFT in some cases showed an overdamped response, which is difficult to model with Eq. (3). Hence, the use of an overdamped second-order model, with the damping ratio fixed to 1 and an additional break frequency as described by Eq. (4), is also considered in this paper.

$$H_{BDFT}(s) = G_{BDFT} \cdot \frac{\omega_{BDFT/1} \cdot \omega_{BDFT/2}}{(s + \omega_{1BDFT})(s + \omega_{2BDFT})} e^{-s\tau_{BDFT}} \tag{4}$$

Fig. 2 shows example BDFT model estimates across four identification runs recorded with the high-intensity multisine motion disturbance for one of the participants exhibiting overdamped BDFT dynamics. The figure shows that for the frequencies of the multisine signal, at which the model is being identified, there is no significant difference in the fit of both models. Using the underdamped model, 72.2% of the BDFT component of the input is modeled for this participant, which becomes 72.4% using the overdamped model. It was therefore concluded that there will be no significant difference in the performance of either model for the cases in which overdamped dynamics are observed. To allow a direct comparison to the work of Khoshnewiszadeh and Pool [13], the underdamped model in Eq. (3) was still used for all further analysis in this paper. See [23] for more details.

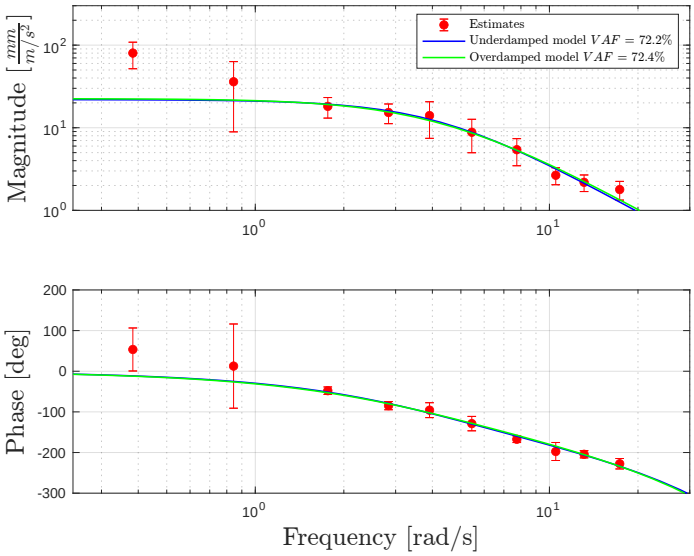

Fig. 2 Comparison between underdamped and overdamped BDFT models resulting from the averaged BDFT estimates of participant 16.

C. Biodynamic Feedthrough Identification

1. Frequency-Domain Identification

Two methods can be used for the identification of the BDFT model: a frequency-domain identification approach also used by Mobertz et al. [14] and Khoshnewiszadeh and Pool [13] and a time-domain approach as, for example, proposed in Zaal et al. [19]. In the frequency-domain identification approach, the BDFT model of Eq. (3) is fitted to a non-parametric estimate of the BDFT frequency response function (FRF), computed from the cross-power spectral density (PSD) of the multisine disturbance and the input signal and the auto-PSD of the disturbance signal, as shown in Eq. (5):

$$\hat{H}_{BDFT}(j\omega_d) = \frac{S_{f''_d u}(\omega_d)}{S_{f''_d f''_d}(\omega_d)} \tag{5}$$

This estimate, although adding estimation errors to the fit, allows for visualizing the frequency response of the estimated BDFT dynamics, giving great insight in the validity of the model structure. The model fit is performed using MATLAB's algorithm *fminsearch*, searching for a set of parameters δ that minimized the normalized magnitude of the error between the model H_{BDFT} and the estimate $\hat{H}_{BDFT}$. The corresponding cost function $J(\delta)$ is defined in Eq. (6):

$$J(\delta) = \sum_{k=1}^{Nd} \frac{|\hat{H}_{BDFT}(j\omega_d) - H_{BDFT}(j\omega_d|\delta)|}{|\hat{H}_{BDFT}(j\omega_d)|} \tag{6}$$

The initial estimate and the constraints used for the optimization of the BDFT model parameters, which were the same for all fitted models, are listed in Table 1.

Table 1 Initial conditions and constraints for BDFT model fitting.

	G_{BDFT} [mm/(m/s^2)]	ω_{BDFT} [rad/s]	ζ_{BDFT} [-]	τ_{BDFT} [s]
Lower limit	0.0	0.0	0.0	0.0
Upper limit	150.0	50.0	2.0	2.0
Initial condition	20.0	6.0	0.6	0.1

2. Time-Domain Identification

Time-domain identification directly fits the model on the BDFT component of the input u^{BDFT}, separated from the voluntary components and from the remnant (this last only for the case of a multisine motion disturbance) using knowledge of the frequencies of target and disturbance signals and the Fourier Transform of the input signal u. The BDFT component of the input u^{BDFT} is then fed to a time-domain estimator, which provides a optimal set of parameters for the parametric model corresponding to a minimum error between the signal u^{BDFT} and the output of the BDFT model, $\hat{u}^{BDFT}$. For this study, a Maximum Likelihood Estimation method is used, as described by Zaal et al. [19].

3. Individual-Run, Subject-Averaged and One-Size-Fits-All Models

For each intensity of the multisine disturbance, a total of four measurement runs were recorded for identification of the model parameters. To understand how much of the BDFT component of the TSC input can be canceled with a model tailored to each of these individual runs, Individual-Run (IR) BDFT models are obtained by fitting the model in Eq. (3) separately to the data of each run. Four IR models are therefore identified per participant per experimental condition. On the other hand, a Subject-Averaged (SA) model was used to describe the average BDFT dynamics of each participant, functioning as a 'personalized' BDFT model. The approach followed to obtain the parameters for the SA models depends on whether a time-domain or a frequency-domain identification approach is used. With the time-domain approach, the parameters of the SA model are the average of the parameters of the fitted IR models. With the frequency-domain identification approach, the SA parameters are obtained by first calculating the non-parametric FRF estimates for each run separately, averaging the FRFs, and fitting a single BDFT model according to Eq. (3) to this FRF. In this two-step identification method, averaging the estimates instead of directly averaging the IR parameters allows to reduce the error introduced during the non-parametric estimation of BDFT. Finally, a One-Size-Fits-All (OSFA) model was obtained by averaging the SA model parameters of all the participants.

III. Methods

The effect of turbulence intensity and variability on BDFT mitigation with a model-based approach were researched by means of an experiment in a moving-base simulator. In the experiment, participants were tasked with following a continuous target on a TSC, while being exposed to heave motion disturbances. The experiment was based on earlier experiments by Mobertz et al. [14] and Khoshnewiszadeh and Pool [13]. This chapter describes the experiment and the data analysis for the current experiment.

Fig. 3 SIMONA Research Simulator, TU Delft.

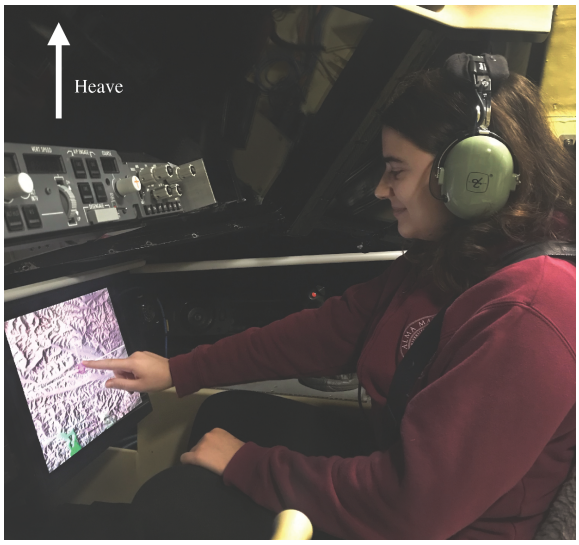

Fig. 4 Experiment set-up.

A. Apparatus

The experiment was conducted using the SIMONA Research Simulator (SRS), a six-degrees-of-freedom moving-base simulator, driven by hydraulic pumps, located at the Faculty of Aerospace Engineering at TU Delft, see Fig. 3. The SRS was equipped with a 15-inch Iiyama Pro-Lite TF1534MC-B1X TSC (1024x768 resolution, 1 pixel = 0.297 mm), mounted as the co-pilot's Primary Flight Display, tilted from the vertical plane with an angle of 18 degrees, see Fig. 4. The drag latency for this TSC with the control task of this experiment is expected to be between 70-80 ms [22].

B. Forcing Functions

1. Control Task

Participants were tasked with a continuous pursuit dragging task, the same as previously used by Khoshnewiszadeh and Pool [13]. The target was shown on the TSC with a target marker (a white triangle), with its location highlighted with a vertical and an horizontal lines intercepting at the marker's location, see Fig. 5. A purple circular marker was shown to provide participants with feedback of the current registered touch location. Fig. 5 also shows the coordinate system used in this paper, as well as a realization of the trajectory of the target trajectory, both of which were not shown to the participants of the experiment, but are included here for clarity. The y and z coordinates of the trajectory of the target marker were generated independently as sums of $N = 3$ sines with different frequencies ω_k, amplitudes A_k, and phases ϕ_k according to Eq. (7). The frequencies of the target signals were chosen to be integer multiples of the base frequency $\omega_m = 2\pi/T_m = 0.0767$ rad/s, derived from the measurement time $T_m = 81.92$ s, to avoid spectral leakage.

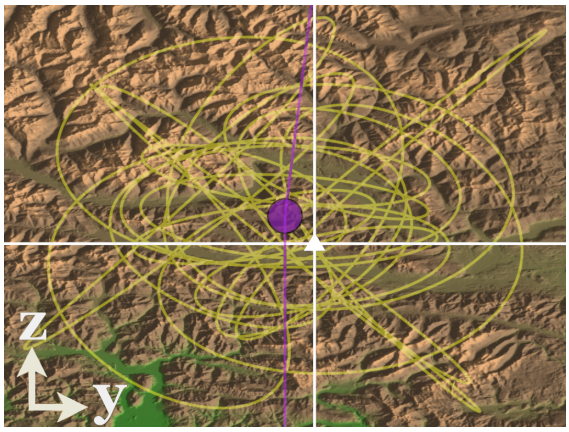

Fig. 5 The display shown to the participants overlaid with a realization of the trajectory of the target (in yellow) and a coordinate system.

$$f(t) = \sum_{k=1}^{N} A_k \sin(\omega_k t + \phi_k) \tag{7}$$

The values used for the construction of f_{ty} and f_{tz} are shown in Table 2 together with the integers n_{ty} and n_{tz} used for the generation of the frequencies ω_k. The spectra of the two target signals are shown in Fig. 6.

Table 2 Values used for construction of the target signal for the TSC tracking task.

	Target, f_{ty}				Target, f_{tz}			
k	n_{ty}	ω_{ty}	A_{ty}	ϕ_{ty}	n_{tz}	ω_{tz}	A_{tz}	ϕ_{tz}
	[-]	[rad/s]	[mm]	[rad]	[-]	[rad/s]	[mm]	[rad]
1	3	0.230	32.767	1.445	2	0.153	22.771	0.308
2	7	0.537	39.777	0.000	13	0.997	39.775	−0.431
3	19	1.457	71.354	−1.825	17	1.304	47.511	−1.591

The use of only three sinusoidal components for each signal was motivated by the need of keeping the task straightforward for the user to perform, while the amplitude of the sines was chosen to fully fill the available screen surface and achieve a representative average finger dragging speed [14]. To prevent recognition of the signal, the lateral and vertical coordinates of the target were flipped, generating a total of four realizations of the target trajectory.

2. Motion Disturbances

In the experiment, three different motion disturbances were compared, next to a reference no-motion (NM) condition: a multisine (M), Gaussian turbulence (G) and Patchy turbulence (P). Each type of motion disturbance (M, G, P) was tested at three different motion intensities (1 = low, 2 = medium, 3 = high), for a total of ten experimental conditions. The intensity of the motion was defined using the root-mean-square (RMS) acceleration level to which participants were

exposed, following up on earlier experiments [6, 24]: $V_{metric} = \sqrt{\ddot{x}_{RMS}^2 + \ddot{y}_{RMS}^2 + \ddot{z}_{RMS}^2}$. As in the current experiment only vertical (heave) accelerations were provided, here $V_{metric} = \ddot{z}_{RMS}$. The three intensity levels used were V_{metric} = 0.75, 0.5, 0.25 m/s^2, implemented by multiplication of the designed high intensity motion disturbance signals with gains of 1, 2/3, or 1/3 respectively, as shown in Fig. 1. The highest intensity selected (V_{metric} = 0.75 m/s^2) corresponds to the intensity of the multisine motion disturbance used in [14] and [13]. No higher intensities were tested to not exceed realistic heavy turbulence levels, as well as the constraints of the motion space of the SRS.

Multisine Motion Disturbance For the multisine motion disturbance, a vertical position disturbance signal was generated as a sum-of-sines signal with a total of $N = 10$ frequency components. These components were selected to cover the range of frequencies at which human BDFT dynamics are relevant and to ensure that the disturbance signal was unpredictable even during repeated exposures [13, 14]. The high-intensity multisine disturbance signal, here referred to as M3, was identical to the signal used in the experiments of [13, 14]; the integers n_d, frequencies ω_d, amplitudes A_d and phases ϕ_d used for each multisine component k are listed in Table 3.

Table 3 Multisine motion disturbance (M3) position signal parameter settings.

k	n_d [-]	ω_d [rad/s]	A_d [m]	ϕ_d [rad]
1	5	0.383	$1.067 \cdot 10^{-1}$	−0.269
2	11	0.844	$8.069 \cdot 10^{-2}$	4.016
3	23	1.764	$4.019 \cdot 10^{-2}$	−0.806
4	37	2.838	$2.048 \cdot 10^{-2}$	4.938
5	51	3.912	$1.246 \cdot 10^{-2}$	5.442
6	71	5.446	$7.568 \cdot 10^{-3}$	2.274
7	101	7.747	$4.735 \cdot 10^{-3}$	1.636
8	137	10.508	$3.424 \cdot 10^{-3}$	2.973
9	171	13.116	$2.856 \cdot 10^{-3}$	3.429
10	226	17.334	$2.416 \cdot 10^{-3}$	3.486

To use this signal on the SRS, both the position and the acceleration signals are required to have a zero starting value. For this reason, the position signal $f_d(t)$ constructed from the values in Table 3 was multiplied with a (half-cosine) fade-in signal with a fade-in time of 8 seconds, and then differentiated twice to obtain the acceleration $f_d''(t)$. More details on the fade-in implementation can be found in Chapter 3 of [23].

Gaussian and Patchy Motion Disturbances The novelty of this paper is that, for the first time, model-based BDFT mitigation is applied to data collected with motion disturbances representative for realistic aircraft responses to turbulence. For this, two motion disturbances were derived from the simulation of the aircraft responses to turbulence, differing in their variability (i.e., patchiness). These conditions were generated using the 'patchy turbulence model' originally created by Van de Moesdijk [25, 26], in the version described in full detail in Chapter 7.2 of [23]. The patchy turbulence model is a stochastic model that generates time traces for the components of an isotropic turbulence velocity field driven by Dryden spectra, tunable to a desirable level of *patchiness*. Patchiness indicates that, in the flow field, areas of high and low energy alternate randomly, introducing spatial variability in the modeled turbulence compared to the conventional linear Dryden spectra. In essence, turbulence is modeled as subsequent patches that are inhomogeneous from patch to patch, but still carry the assumptions of homogeneity and stationarity within each patch [25].

A total of four parameters are used to tune the patchy turbulence model. The isotropic turbulence intensity σ_g^2 and the longitudinal integral length scale L_{u_g} define the power spectrum of the resulting turbulence. The model's Q and R parameters control its patchiness. Q, varying between 0 and +∞, specifies the Kurtosis of the probability density function (PDF) of the components of the turbulence velocity field. With $Q = 0$, a Gaussian distributed turbulence velocity profile is obtained, with time-invariant characteristics. Setting $Q > 0$, the Kurtosis of the PDF is increased, leading to a higher occurrence of turbulence having high and low velocities, increasing its variability [26]. For reference, a Kurtosis up to $K = 6$ has been observed in atmospheric turbulence [26]. The R parameter can vary between 0 and 1 and is used to model the variability of turbulence in the pilots' perception, specifying the scale of a patch of turbulence in comparison to the integral scale of the largest eddies in the turbulent flow [26]. In particular, $R = 1$ indicates short patches, which increase in length as R decreases [26].

In the experiment, data was collected for two realistic turbulence conditions: a time-invariant turbulence, having a Gaussian distributed PDF of the turbulence velocities, named the Gaussian condition (G) and a time-varying turbulence with patchy characteristic, the Patchy condition (P). The parameter settings of the patchy turbulence model for the two conditions can be found in Table 4.

Table 4 Input parameters for the patchy turbulence model to generate the Gaussian and Patchy turbulence used in this experiment.

Condition	σ_g^2 [m^2/s^2]	L_{u_g} [m]	Q [-]	R [-]
Gaussian (G)	1	300	0	-
Patchy (P)	0.5	300	1.55	0.1

Both Gaussian and Patchy turbulence conditions just mentioned led to an overall motion intensity of V_{metric} = 0.75 m/s^2, as simulated by the SRS. The selection of two different values for the turbulence intensity parameter σ_g^2 and of the motion filter settings (that will be described in the remainder of the section) are driven by the need of simulating motion with the selected V_{metric}.

The output of the turbulence model was filtered with a second-order low-pass filter with a cut-off frequency of 10 Hz, both because the Dryden spectra used for the turbulence model deviate from the spectra of actual turbulence at high frequencies [24, 27], and because of the physical limitations of the simulator, which would be damaged if exposed to high frequency motion. The symmetric components of the turbulence velocity field generated using the patchy turbulence model were then fed to a Cessna Citation 500 non-linear model based on the DASMAT architecture (see Van der Linden [28]) to simulate the vertical aircraft response to the designed turbulence. The antisymmetric turbulence velocity field was neglected, as it has negligible influence on symmetric aircraft motion. The aircraft model was then linearized for straight level flight at an altitude of 28,000 ft (8534.4 m), flying at a velocity of V = 165 m/s and having initial mass of 4,000 kg, equivalent to [24].

The output of the aircraft model was passed through a motion filter, the classical washout filter (CW16), to simulate the vertical aircraft response with the SRS. Here, all motion except for the vertical accelerations was discarded, and these accelerations were filtered to remove the low-frequency components of the motion using a third-order high-pass motion filter. To achieve this while avoiding confounds, the same filter settings were used for both the Gaussian and the Patchy conditions. Of these settings, the damping ratio was fixed to 0.7, the first-order pole to 0.2 rad/s, following the specification in [29]. The gain K_{heave} = 1 and break frequency of the second-order pole ω_{heave} = 0.9 rad/s were selected after performing a simulator workspace analysis [29], in which the parameters were optimized to simulate the motion of the aircraft within the constrains of the simulator workspace as closely as possible for the selected highest motion intensity V_{metric} = 0.75 m/s^2. In the selection of the motion filter settings, the break frequency of the high-pass frequency was selected as low as possible within all other constraints, to simulate the motion at frequencies overlapping as much as possible the frequency band of the multisine. The details of the algorithm used can be found in [29], while the details of the selection of the parameters of the turbulence model, aircraft model and filter settings can be found in Chapters 7.1 and 7.4 of [23].

Experiment Conditions The spectra of all different disturbance signals are shown in Fig. 6 together with the y and z target signals. In addition, Fig. 7 zooms in on the time traces of the vertical acceleration for the three high-intensity conditions. The higher turbulence variability of the Patchy condition with respect to the Gaussian condition can be seen in the peaks present in the vertical acceleration (examples around 3, 10, 20 seconds), while the smoothness of the multisine disturbance clearly shows a lack of high frequency components in this signal. This difference is measurable by calculating the crest factor CF: for Gaussian turbulence signal CF = 3.23, while for the Patchy case CF = 3.82.

Summarizing, a total of 10 conditions are tested in the experiment, as listed in Table 5. The M3 condition corresponds to the motion disturbance used in [13], and as such is also referred to as baseline. For the Gaussian conditions, an offset of maximum 0.02 m/s^2 can be observed in the exact value of V_{metric} calculated in the accelerations used during the experiment. This offset is due to the fact that the accelerations of the simulator for the turbulence cases were the output of an optimization on the parameters of the turbulence velocity field, those of the simulated aircraft and of the motion filters. Parameter outcomes of the optimization resulting in V_{metric} close enough to the target were used, as an offset of 0.02 m/s^2 is believed to not influence results.

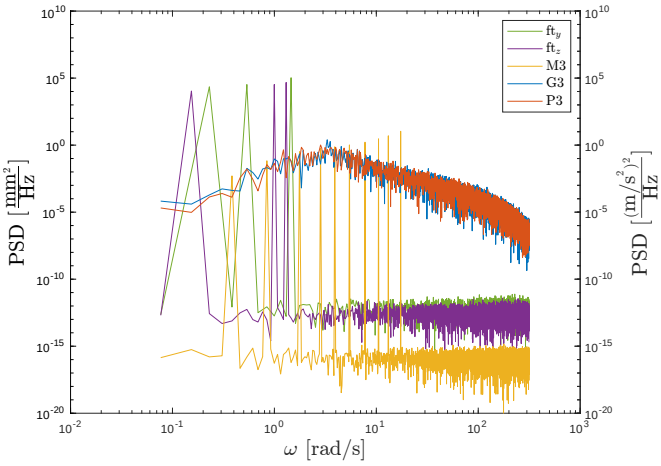

Fig. 6 PSD of the TSC target and motion disturbance signals; f_{ty} and f_{tz} refer to the left axis with units mm^2/Hz; M3, G3, P3 to the right axis, with units $(\text{m/s}^2)^2/\text{Hz}$.

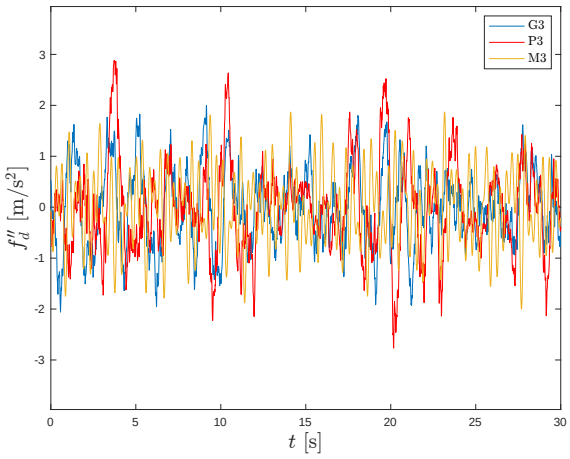

Fig. 7 Detail of the time traces of the multisine, Patchy and Gaussian conditions, V_{metric} = 0.75 m/s^2.

Table 5 Experimental conditions matrix.

Condition	Description	V_{metric} [m/s^2]
NM	No motion	-
M1	Multisine low intensity	0.25
M2	Multisine medium intensity	0.50
M3	Multisine high intensity	0.75
G1	Gaussian low intensity	0.24
G2	Gaussian medium intensity	0.48
G3	Gaussian high intensity	0.73
P1	Patchy low intensity	0.25
P2	Patchy medium intensity	0.50
P3	Patchy high intensity	0.75

C. Participants

A total of 21 volunteers, 15 male and 6 female, took part in the experiment. Participants were all right handed, between 19 and 33 years of age (μ = 23.8 years, σ = 3.8 years) with height between 1.67 and 2.03 m (μ = 1.78 m, σ = 0.08 m) and weight between 51 and 102 kg (μ = 74.2 kg, σ = 12.8 kg). All participants reported having at least 8 years of experience using TSCs.

D. Procedures

Participants were informed that the experiment was performed to better understand the effects of turbulence on the use of TSCs in aircraft cockpits. No explicit details were given on the different motion conditions that would be tested, neither in regards to the intensity nor to the types of motion disturbances. They were instructed to perform the tracking tasks described in Section III.B, by following the white marker and lines with their index finger, and were told that the purple marker was shown to provide feedback. Participants were instructed to adjust their seating position and height before the start of the experimental runs to perform the tracking task with their backs upright and their arms in a natural (not too close, not outstretched) position with respect to the TSC.

Once a seating position was fixed, participants were told to maintain that position throughout the experiment. In addition, participants were instructed to not lift their hand from the surface of the screen for the duration of the experimental runs. To reduce friction between the participant's skin and the TSC surface, and preventing them from experiencing excessive fatigue, the participants wore anti-static gloves. Noise-canceling headphones were used to mask the sounds made by the hydraulic motion actuators, preventing participants from predicting the simulator's accelerations.

Each participant was familiarized with the control task both with and without motion, and at different motion intensities during a fixed program of four training runs (NM, M1, M2, M3). Subsequently, data were collected for 16 trials to be used for the identification of the BDFT model and 36 trials to be used for the evaluation of the cancellation performance. The order of execution of the combined 52 identification and cancellation runs was randomized for each participant. To allow participants to rest, three breaks of 15 minutes were planned, for a total experiment duration of 3 hours. The 16 identification trials comprised of conditions M1, M2, M3 and NM, repeated four times each. The 36 evaluation trials comprised all conditions except for the NM condition (M1, M2, M3, G1, G2, G3, P1, P2, P3), again repeated four times each. For each repetition of the trials, the sign of one or both of the coordinates of the target signal on the TSC was flipped, reducing the chance that the participant could recognize and anticipate the movement of the target on the screen.

Participants were informed of the total (expected) duration of the experiment, of the three 15 minutes breaks and of the duration of each run. They were also told and encouraged to take short breaks in between runs (while remaining in the simulator) to rest their arms when needed, and of the possibility to take breaks outside of the simulator upon their request. Participants were instructed to give notice to the experimenter in case of motion sickness, ensuring that no data would be collected and used for the analysis if participants were not feeling well.

The experiment and procedures were approved by the TU Delft's Human Research Ethics Committee (HREC) under application number 1734. Participants signed an informed consent form ensuring their understanding of the experiment procedures, the safety and emergency procedures onboard the SRS, their rights of withdrawal from the experiment, and of the subsequent publication of the anonymized data in individual or aggregated form.

E. Hypotheses

The following hypotheses were formulated for the experiment:

H1: *Over 90% of the BDFT component of the TSC input occurring with the multisine motion disturbance at high intensity (M3, $V_{metric} = 0.75$ m/s^2) will be accounted for with personalized BDFT models.* The identification of BDFT with a high-intensity multisine disturbance signal is essentially a direct replication of the experiment of Khoshnewiszadeh and Pool [13]. It is therefore expected that the BDFT identification results for the M3 condition, when personalized to each participant, will have comparable accuracy to the results reported in [13].

H2: *A BDFT model identified for a higher motion intensity (V_{metric}) will overestimate BDFT when applied to data for a lower V_{metric} setting. Mitigating BDFT on data collected at a specific V_{metric} using a BDFT model identified at the same V_{metric} will lead to comparable performance, independent of the magnitude of V_{metric}.* The main effect on BDFT of a decrease in the intensity of the disturbance motion is expected to be a decrease in the magnitude of the BDFT component of the TSC input. It can be hypothesized that the gain encoding the proportionality between motion disturbance input and BDFT output will be higher for the high motion intensity case compared to the ones for the medium and low motion intensity cases. Therefore, the BDFT model identified at high intensity is expected to overestimate the amount of BDFT present at medium and low motion intensities, and *vice versa*. Since the identification and mitigation techniques and the type of data used at the high motion intensity are the same as the ones used for the lower motion intensities, it is hypothesized that BDFT mitigation tailored for each intensity will result in comparable performance.

H3: *A more compliant control behavior of the TSC operators, i.e., a lower natural frequency in their BDFT dynamics, will be observed with disturbances caused by Gaussian turbulence, when compared to the multisine disturbance. Effective model-based BDFT mitigation can still be obtained by adapting the BDFT model parameters accordingly.* Comparing the time traces of the motion disturbances in Fig. 7, a higher amount of high frequency motion is visible in the Gaussian and Patchy cases when compared to the multisine. This is further confirmed by their power spectra in Fig. 6. These high frequency components continuously perturb the participants' control action. Hence, the Gaussian motion disturbance is expected to induce participants to keep their muscles more relaxed than for the corresponding multisine conditions. The reduced rigidity will cause less feedthrough of high frequency acceleration components. Adaptation of the parameters of a BDFT model identified for participants with a multisine disturbance signal is expected to suffice to still attain effective mitigation.

H4: *A time-varying neuromuscular adaptation will be observed with motion disturbances caused by Patchy turbulence. Low performance will be observed with model-based BDFT mitigation using a linear time-invariant BDFT model.* The accelerations caused by Patchy turbulence (turbulence of variable nature) present variations in time in their magnitude, shown visually using Fig. 7 and quantified through a crest factor, see

Section III.B.2. Consequently, it is expected that the participants exposed to such disturbance will adapt their control behavior throughout the measurement time, to maintain a good performance in the tracking task. Due to this expected time-varying characteristic of participants' BDFT dynamics, time-invariant BDFT models will show reduced accuracy and provide less effective BDFT mitigation.

F. Dependent Measures

During the experiment, the lateral and vertical components of the TSC input provided by the participants were collected with a sampling frequency of 100 Hz, together with the motion disturbances and target signals shown on the TSC. In addition, participants were asked to provide their age, weight, height and years of experience with TSCs, and to notify the experimenter if contact with the screen was lost during a measurement trial. From the collected data, a number of dependent measures were calculated to test the hypotheses:

- BDFT model parameters: G_{BDFT}, ω_{BDFT}, ζ_{BDFT}, τ_{BDFT}. These are used to explicitly quantify the effects of different motion disturbance intensities on the BDFT dynamics, as well as to understand differences in the BDFT dynamics of different participants. Furthermore, the estimated parameters are also used to compare the different BDFT dynamics occurring under multisine motion disturbance or Gaussian and Patchy turbulence motion disturbances.
- Variance Accounted For: VAF. This metric is used to evaluate the performance of model-based BDFT mitigation, quantifying how much of the involuntary component of the input signal u^{BDFT} is modeled by the BDFT model. For the multisine case, in which $u^{BDFT} = u^{BDFT}_{f''_d}$, the metric exploits the characteristic of the signal, in which disturbance components, control task components and remnant are clearly distinguishable:

$$VAF_M = \sum_{f''_d} \left(1 - \frac{Var(u^{BDFT}_{f''_d} - \hat{u}^{BDFT}_{f''_d})}{Var(u^{BDFT}_{f''_d})} \right) \times 100\% \tag{8}$$

  For the TSC inputs recorded under Gaussian and Patchy turbulence, where it is not possible to separate the BDFT component from the remnant, BDFT mitigation performance is evaluated on all frequencies except for the lateral and vertical target frequencies. To somewhat compensate for the contribution of the remnant, the TSC input recorded in static conditions at these frequencies u^{NM}_f is subtracted from the TSC input signal u_f recorded in Gaussian and Patchy conditions:

$$VAF_{G/P} = \sum_{f \neq f_{ty}, f_{tz}} \left(1 - \frac{Var(u_f - u^{NM}_f - \hat{u}^{BDFT}_f)}{Var(u_f - u^{NM}_f)} \right) \times 100\% \tag{9}$$

  For both versions of the metric, the VAF is used to evaluate the identification performance, i.e., how much of the BDFT signal is accounted for by the model. VAF = 100% indicates a perfectly modeled signal, with decreasing modeling performance as the VAF decreases. Given the presence of remnant in the $VAF_{G/P}$ used for Gaussian and Patchy conditions, this metric is to be interpreted more as an index of identification performance rather than as an explicit quantification of the amount of modeled feedthrough.
- Cancellation Index (CI). This metric is used to quantify the performance of the SA and OSFA BDFT models for the cancellation of BDFT in the evaluation data set. As for the VAF, two versions of this metric are used, one applicable to BDFT with any type of motion disturbance, CI in Eq. (10), and one specific for BDFT due to a multisine motion disturbance, CI_M in Eq. (11).

$$CI = -\sum_{f \neq f_{ty}, f_{tz}} \left(1 - \frac{Var(u_f - u^{NM}_f - \hat{u}^{BDFT}_f)}{Var(u_f - u^{NM}_f)} \right) \times 100\% \tag{10}$$

$$CI_M = -\sum_{f''_d} \left(1 - \frac{Var(u^{BDFT}_{f''_d} - \hat{u}^{BDFT}_{f''_d})}{Var(u^{BDFT}_{f''_d})} \right) \times 100\% \tag{11}$$

  For both, the BDFT component of the input signal is fully canceled when CI = -100%, with smaller negative values indicating a lower cancellation performance. A positive value for CI indicates that the BDFT mitigation applied is actually increasing the input contribution due to acceleration feedthrough rather than decreasing it. When applied to the same data, it should be noted that CI_M = -VAF_M and CI = -$VAF_{G/P}$.

- BDFT modeling error $e(t)$. Defined as the absolute value of the difference between the BDFT component of the input recorded during the experiment and its modeled counterpart, this metric is used to reveal any time-varying fluctuations in BDFT modeling errors for the time-varying Patchy turbulence conditions.

$$e(t) = \left| u^{BDFT}(t) - \hat{u}^{BDFT}(t) \right| \tag{12}$$

Lower than expected performance in the identification of the BDFT models for the multisine conditions prompted the evaluation of additional dependent variables, which were used to explain the findings. The additional metrics used are reported below:

- Run variability RV. This metric is used to quantify the variability in the BDFT component of the TSC input u^{BDFT} across the repeated measurement runs of a specific participant. The variability is calculated using Eq. (13):

$$RV(i,j) = 100 - \sum \left(1 - \frac{Var(u^{BDFT}(i) - u^{BDFT}(j))}{Var(u^{BDFT}(i))} \right) \times 100\% \tag{13}$$

  The quantity RV is a three-by-three matrix, for each element of which the indices i and j indicate two of the four experimental runs, therefore $1 < i < 4$, $1 < j < 4$ and $i \neq j$. If the BDFT components in run i and in run j are exactly the same, $RV(i,j) = 0\%$. The metric RV is therefore close to zero when the BDFT components of two runs are consistent and have a higher value when there is a lot of variability. Two elements of the matrix will therefore be calculated for each two experimental runs, $RV(i,j)$ and $RV(j,i)$. The average of these two elements is used as the estimated variability across the two runs i and j.
- Relative remnant ρ_u^2. This metric is used to quantify the linearity of the BDFT measured in the multisine cases. This is done by calculating the (signal-to-noise) ratio between the remnant contribution in the TSC input signal at the frequencies of the disturbance signal, $\tilde{S}_{uu,n}(j\omega_d)$, and the measured contribution of the BDFT component itself, $S_{uu}(j\omega_d)$:

$$\rho_u^2(j\omega_d) = 1 - \frac{\tilde{S}_{uu,n}(j\omega_d)}{S_{uu}(j\omega_d)} \tag{14}$$

  The estimated remnant power at the frequencies of the disturbance signal $\tilde{S}_{uu,n}(j\omega_d)$ was calculated, making the assumption of smooth variations in the power of the remnant across adjacent frequencies, as the average of the remnant power at frequencies in the neighbor of the disturbance frequencies. A value of ρ_u^2 close to zero indicates a low signal-to-noise ratio, in which the remnant dominates over the acceleration feedthrough. On the other hand, $\rho_u^2 = 1$ indicates a perfectly linear transmission, on which no remnant is present.

IV. Results

The results presented in this section are divided in five parts, connected to the hypotheses formulated before the start of the experiment. These relate to the identification of BDFT using the multisine, high intensity runs (M3 condition, Section IV.A), the identification accuracy and mitigation performance of a BDFT model at low and medium intensity (M1 and M2 conditions, Section IV.B), identification and mitigation of BDFT occurring with time invariant turbulence (G3 condition, Section IV.C) and the effect of variability on model-based BDFT mitigation (P3 condition, Section IV.D). In addition, results for the Gaussian and patchy conditions at lower intensities are discussed in Section IV.E.

A. Biodynamic Feedthrough Identification at the Baseline High-Intensity Multisine Condition

1. Comparison with previously collected data

Fig. 8 shows the BDFT model accuracy for the baseline M3 condition (VAF_M, Eq. (8)) for each participant. In this figure, both the VAF_M for the dataset collected in the current paper (21 participants) and for the dataset collected in [13] (18 participants) are shown. In the left panel, the mean performance across runs for each participant is indicated with a thick line, while the shaded area shows the corresponding standard deviation. The right panel shows the Subject-Averaged results in a boxplot.

For the current experiment's M3 data, the median VAF_M was found to be 87.1%, which is 5.6% lower compared to Khoshnewiszadeh and Pool's dataset (92.7%). The difference in identification performance was confirmed to be statistically significant using a non-parametric Wilcoxon signed-rank test ($p < 0.01$). To infer the causes of the difference between the two datasets, the variability across the BDFT components of the TSC input recorded during the four

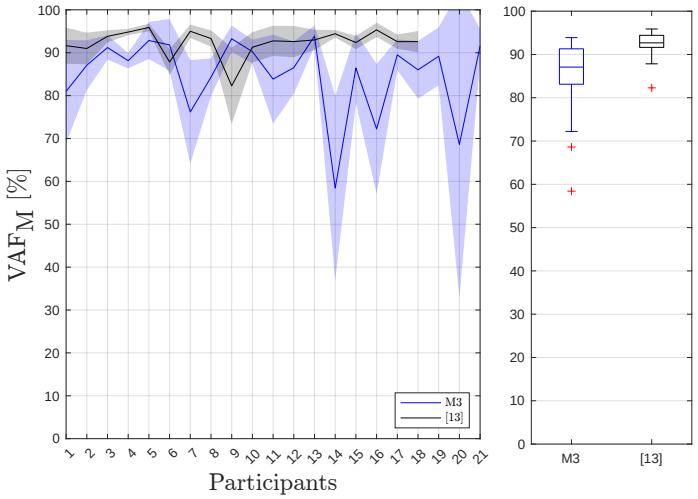

Fig. 8 Performance of the identification of BDFT (time domain approach, SA model).

identification runs was quantified using the RV metric defined in Eq. (13). Fig. 9 and Fig. 10 show, for each participant of the M3 dataset of this experiment and of Khoshnewiszadeh and Pool's dataset, respectively, a boxplot of all RV values, averaged across all combinations of two runs. The higher the median, the less consistency in the measurements obtained from the participant.

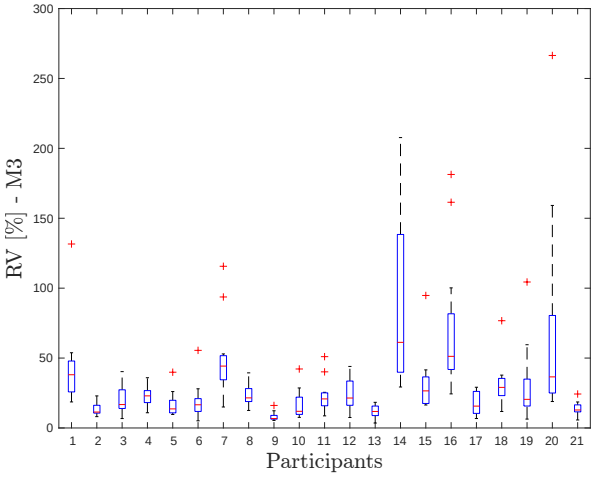

Fig. 9 Variability across measurement runs, M3 condition.

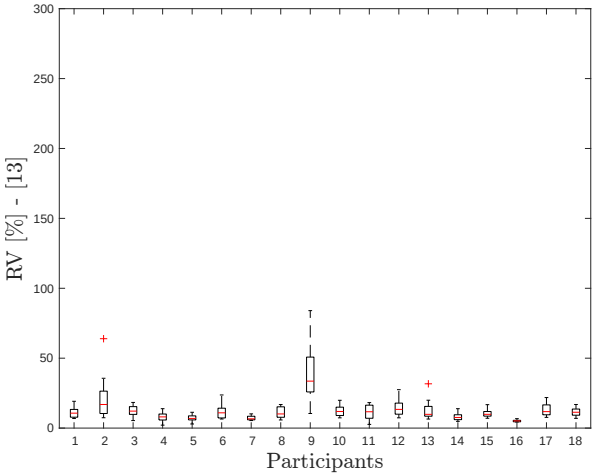

Fig. 10 Variability across measurement runs, Khoshnewiszadeh and Pool's data [13], M3 condition.

Comparing identification performance and variability for the M3 dataset, respectively, in Fig. 8 and Fig. 9, it can be seen that participants with the lowest VAF_M (participants 7, 14, 16, and 20, all with a median VAF_M below 80%) also show inconsistent BDFT across runs, with a high median and spread. Although on average the data from [13] is markedly more consistent, the same correlation is also visible for this previous dataset, e.g., see participant 9 in Fig. 10. The increased BDFT variability in the M3 condition is likely explained by the longer duration of the current experiment (56 measurement runs, compared to 16 for [13]). Fatigue and boredom may have caused participants to be less consistent in performing the tracking task over the time-span of the experiment, for example changing their neuromuscular dynamics to minimize fatigue.

2. Comparison of One-Size-Fits-All, Subject-Averaged and Individual-Run models

Fig. 11 shows the BDFT model accuracy, again expressed as VAF_M, for the fitted IR (green), SA (blue) and OSFA (red) models applied to all individual runs of all participants for the M3 data. This comparison was performed to verify the effect of different levels of individualization on BDFT modeling performance.

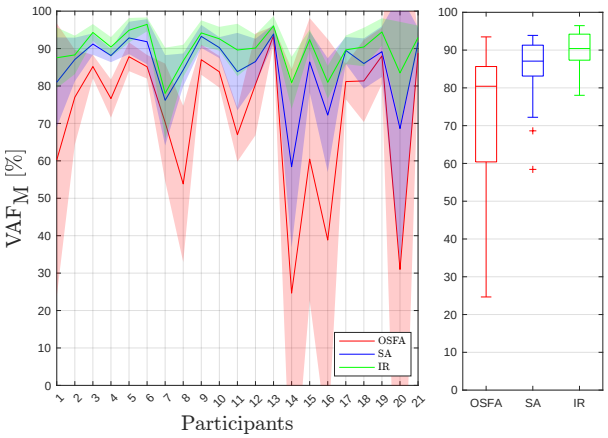

Fig. 11 Performance of the OSFA, SA and IR $H_{BDFT/M3}$ models for the identification of BDFT.

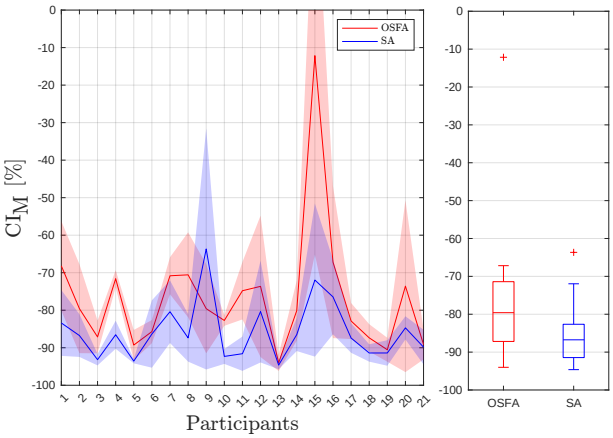

Fig. 12 Cancellation performance of OSFA and SA $H_{BDFT/M3}$ models on BDFT occurring in M3 condition.

Clearly, the more a BDFT model is tailored to each specific data set, the better it describes this data. The OSFA model gives a median VAF_M of 80.4%, which is considerably lower than obtained with SA (87.1%) and IR (90.4%) models. A Friedman test confirmed these differences to be highly significant ($p < 0.01$). Post-hoc Wilcoxon signed-rank tests confirmed the significance of the difference across all subsets ($p < 0.01$). Notably, the largest improvement in identification performance with the IR model is visible for participants who have comparatively low performance for the SA model, such as participants 14, 16 and 20; these are also the participants who show the highest degree of variability across runs, see Fig. 9.

Fig. 12 shows the corresponding cancellation performance achieved when applying the OSFA and SA $H_{BDFT/M3}$ models to the independent validation dataset. This figure shows the CI_M index as defined in Eq. (11). Using the OSFA model on this dataset, up to 79.6% of the BDFT input contribution is canceled, only 0.8% less than the performance of this model on the identification dataset, see Fig. 11. With the SA model, a median performance of CI_M = -86.8% is achieved, differing from identification performance by only 0.3%, with one outlier. These results prove that the effects of the variability between participants are in general much larger than the between-run variability. In fact, only for a single participant (participant 9) the variability in BDFT dynamics was high enough to cause the OSFA model to perform better than the personalized SA model.

B. Performance of Biodynamic Feedthrough Mitigation at Different Intensities

Fig. 13 and Fig. 14 show the performance of the identification of the OSFA, SA, IR BDFT models for the M2 condition ($H_{BDFT/M2}(j\omega)$) and for the M1 condition ($H_{BDFT/M1}(j\omega)$), respectively. These figures show exactly the same data and use the same format as Fig. 11, which shows the M3 condition's results.

For the $H_{BDFT/M2}$ models, the identification performance is found to be comparable to the performance of $H_{BDFT/M3}$, see Fig. 11, for all three model types. The OSFA model captures up to 81.0% of the BDFT input components (+0.6% compared to $H_{BDFT/M3}$); for SA models this becomes 87.3% (+0.2%) and for IR models 90.4% (+0%). Differences in performance of the identification of the OSFA and SA $H_{BDFT/M2}$ and $H_{BDFT/M3}$ models were confirmed to be statistically insignificant with Wilcoxon signed-rank ($p \geq 0.05$). With the IR model, the Wilcoxon signed-rank reported significant differences ($0.01 \leq p < 0.05$), which are due to the larger spread across participants in the identification performance, see the green boxplots in Fig. 11 and Fig. 13.

The identification of $H_{BDFT/M1}$ gave considerably less accurate results compared to $H_{BDFT/M2}$ and $H_{BDFT/M3}$: 68.5% with the OSFA model (-11.9% compared to $H_{BDFT/M3}$ and -12.5% compared to $H_{BDFT/M2}$), 74.0% with the SA model (-13.1% compared to $H_{BDFT/M3}$ and -13.3% compared to $H_{BDFT/M2}$) and 78.3% with the IR model (-12.1% compared to both $H_{BDFT/M3}$ and $H_{BDFT/M2}$). For all three types of models, the differences in performance

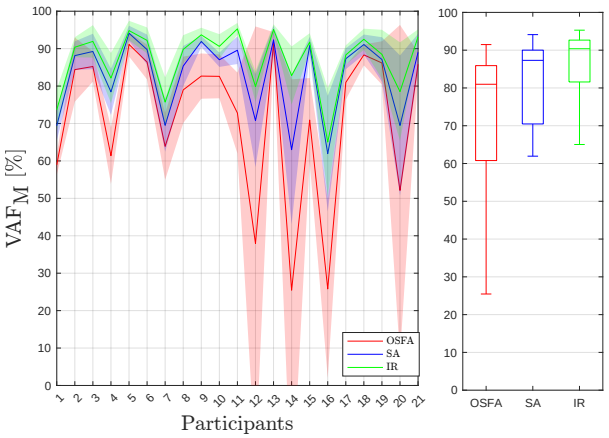

Fig. 13 Performance of the OSFA, SA and IR $H_{BDFT/M2}$ models for the identification of BDFT from the M2 data.

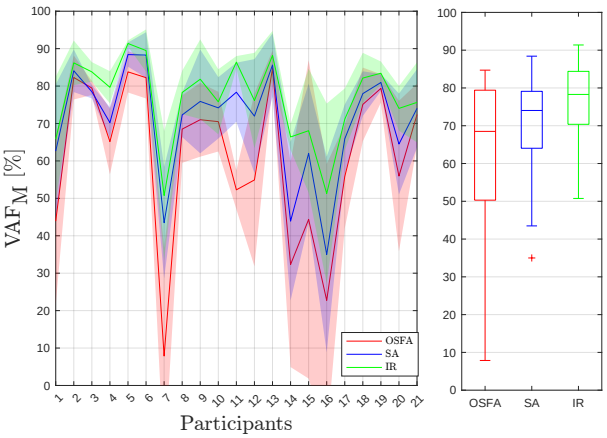

Fig. 14 Performance of the OSFA, SA and IR $H_{BDFT/M1}$ models for the identification of BDFT from the M1 data.

were shown to be highly significant (Wilcoxon signed-rank test, $p < 0.01$). To explain these differences in identification performance, the reliability of the identification of the BDFT model at the motion intensities tested during the experiment was compared as a function of frequency using the relative remnant ρ_u^2 defined in Eq. (14). The results of this analysis for the three intensity levels are shown in Fig. 15, where the thin lines represent individual participant results, and the thick lines with circular markers their averages.

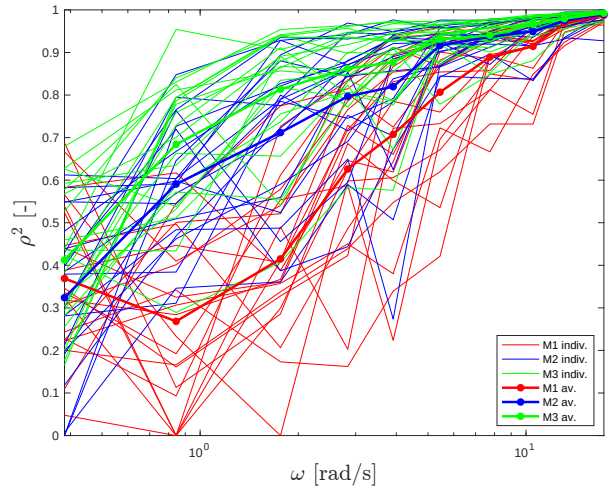

Fig. 15 Relative remnant across intensities, showing contribution of individual participants and their average.

Fig. 15 shows that at high frequencies ρ_u^2 is close to 1 for all three motion intensities, indicating that the contribution of the remnant is negligible, and that the BDFT dynamics are approximately linear. The relative remnant, however, decreases with decreasing frequency, more steeply for the progressively lower intensities. This indicates that at low frequencies the BDFT measurement suffers from a low signal-to-noise ratio (SNR): there is simply not much feedthrough occurring at the low-intensity low-frequency perturbation frequencies, confirming that BDFT is a high-frequency phenomenon. This trend occurs more strongly for the medium and low motion intensities, as the magnitude of the feedthrough occurring at those intensities is lower throughout the entire frequency range compared to the M3 case.

To further verify this, the corresponding parameters of the BDFT models identified at the different intensities were compared. Fig. 16 shows, for the three motion intensities tested, the median and spread of the parameters of the SA BDFT model across participants, as well as their averages (i.e., the OSFA model, displayed with diamond markers).

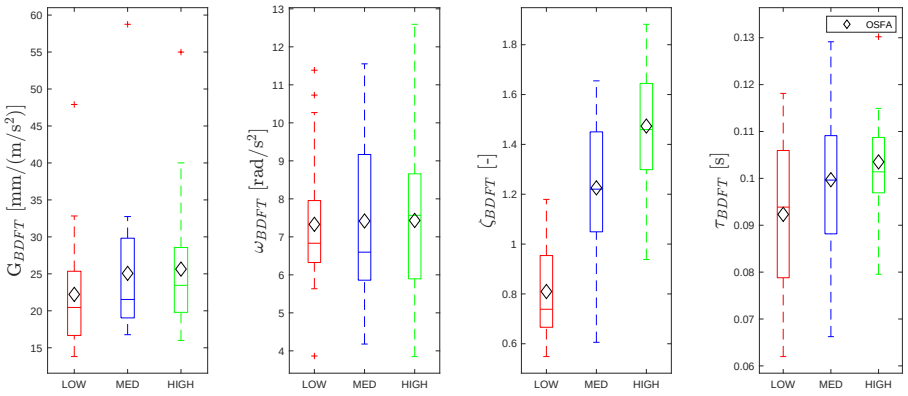

Fig. 16 Median and spread of the parameters of the $H_{BDFT/M}(j\omega)$ models across intensities (SA and OSFA models).

The first panel from the left of Fig. 16 shows a small decrease in the median of the gain G_{BDFT} with decreasing intensity, with the spread remaining roughly constant. In the M1 condition G_{BDFT} is 13% lower than in the M3 condition, and in M2 8% lower than in M3. Differences in median and spread of the break frequency ω_{BDFT} (second panel) are small and inconsistent (10% lower in M1 compared to M3, 13% lower in M2), hinting that (unexpectedly) no changes in neuromuscular stiffness occur across the three intensities tested. The damping ratio ζ_{BDFT} shown in the third panel of Fig. 16 decreases with decreasing intensity; the median values of ζ_{BDFT} found for M1 and M2 are, respectively, 49% and 16% lower than in M3. Also the time delay τ_{BDFT} (fourth panel) slightly decreases with decreasing motion intensity, with a 7% and a 2% decrease compared to M3 in M1 and M2 cases, respectively. However, while for ζ_{BDFT} the spread is unchanged across intensities, a very clear decrease in spread is visible for the time delay τ_{BDFT} with increasing intensity. At low intensity the spread of the time delay is larger, likely because the low SNR causes the estimation of this parameter to be inaccurate. To further visualize these results, a Bode plot with the BDFT estimates (lines) across intensities is shown in Fig. 17 together with the frequency responses of the BDFT models identified for individual participants (asterisks), grouped per intensity by color.

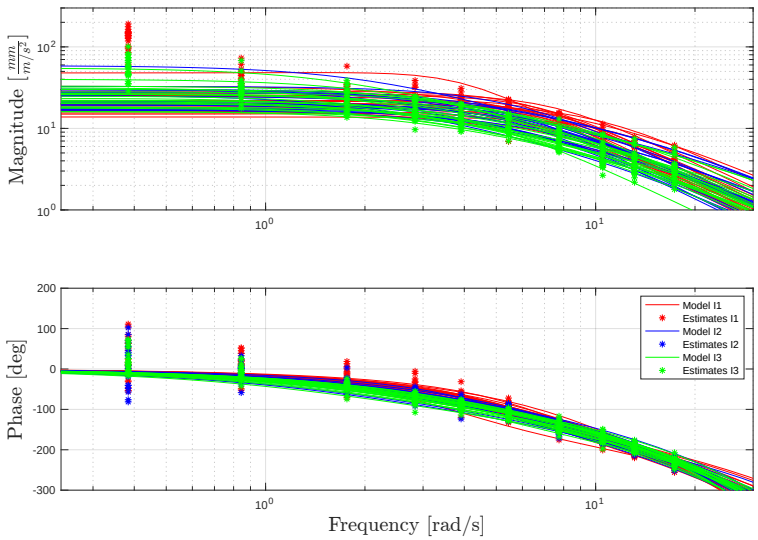

Fig. 17 BDFT estimates and frequency response of the BDFT models of individual participants across intensities (SA model).

Fig. 17 shows no clear differences in the gain, break frequency and in the time delay constants across intensities, consistent with Fig. 16. Differences in the damping ratio are instead very visible, especially in the phase shift. In fact, the phase shift increases with increasing intensity over the frequency range characterizing the damping of the response,

suggesting that it will not be possible to use a single model for mitigation of BDFT across intensities. To confirm these findings, the performance of the cancellation of BDFT occurring at the low and medium intensities was cross-validated with the model identified from the high intensity accelerations, and compared to the performance of BDFT models identified from low- and medium-intensity data. Fig. 18 shows the cancellation performance (calculated using the multisine specific CI_M in Eq. (11)) of the SA BDFT model identified at the high motion intensity $H_{BDFT/M3}(j\omega)$ and of the SA BDFT model identified at the medium motion intensity $H_{BDFT/M2}(j\omega)$, on the M2 data. Similarly, Fig. 19 compares cancellation performance on the M1 data of the high-intensity and the low-intensity SA models, $H_{BDFT/M3}(j\omega)$ and $H_{BDFT/M1}(j\omega)$ respectively.

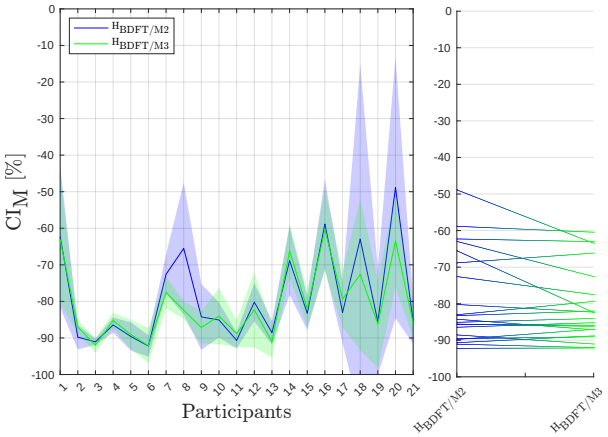

Fig. 18 Cancellation performance of models $H_{BDFT/M3}$ and $H_{BDFT/M2}$ on BDFT occurring in condition M2 (SA model).

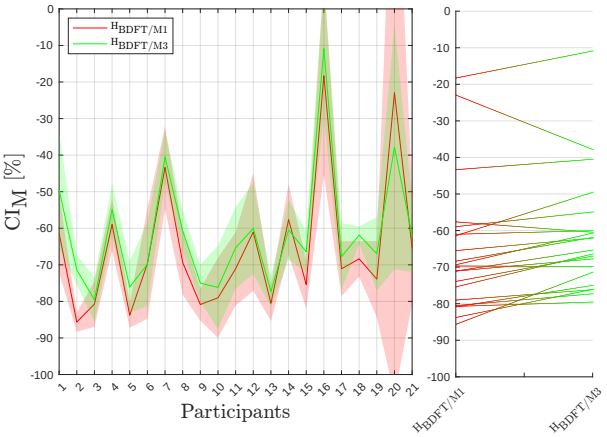

Fig. 19 Cancellation performance of models $H_{BDFT/M3}$ and $H_{BDFT/M1}$ on BDFT occurring in condition M1 (SA model).

Fig. 18 shows that the two models have roughly the same performance on the M2 data. For $H_{BDFT/M2}(j\omega)$, a median CI_M of -84.2% is canceled across participants, while using $H_{BDFT/M3}(j\omega)$ the median cancellation index is -84.0%. This difference was not statistically significant (Wilcoxon signed-rank test, $p \geq 0.05$). Hence, the model identified for the high-intensity M3 case can be used effectively for BDFT cancellation in the medium intensity (M2) case. For the low intensity model $H_{BDFT/M1}(j\omega)$ (Fig. 19) a median CI_M of -69.7% is reached, with the median of $H_{BDFT/M3}(j\omega)$ at CI_M = -65.4%. The difference between the two models is highly significant ($p < 0.01$) in this case. The performance of the $H_{BDFT/M3}(j\omega)$ model on the M3 data (-86.8%, see Fig. 12), of the $H_{BDFT/M2}(j\omega)$ model on the M2 data (-84.2%) and of the $H_{BDFT/M1}(j\omega)$ model on the M1 data (-69.7%) was compared using Friedman's test and with post-hoc Wilcoxon signed-rank tests. These showed a statistically significant difference between the first two (M3 and M2, $0.01 \leq p < 0.05$), and a highly significant difference for all other combinations ($p < 0.01$). Overall, this confirms that at lower intensities, identification of the BDFT model is simply less accurate. Equivalent results were obtained for the same analysis applied to the OSFA models obtained for M3, M2, and M1 (see [23] for details).

C. Biodynamic Feedthrough Mitigation in Gaussian Turbulence

To evaluate whether model-based BDFT identification can also be effective with realistic (non-multisine) turbulence signals, the parametric BDFT model was also fitted to an estimate of the BDFT component in the TSC input recorded at the high intensity Gaussian condition (G3). This estimate of BDFT was obtained by removing the multisine components from the vertical and horizontal target signals from the vertical TSC input. The time-domain identification algorithm described in Section II.C.2 was used to fit the BDFT model parameters, keeping in mind that with motion disturbance other than multisine signals, BDFT cannot be separated from the remnant, as they both contribute to the power of the signal across the entire frequency spectrum. To prevent noise from affecting the estimation of the time delay, τ_{BDFT} was fixed to the values obtained through the identification of the SA BDFT model with the multisine signal for the SA and IR models, and of the OSFA BDFT model for the OSFA case. The performance of the identification of the $H_{BDFT/G3}$ model was evaluated using the $VAF_{G/P}$ metric defined in Eq. (9), and is shown in Fig. 20 for the OSFA, SA and IR models.

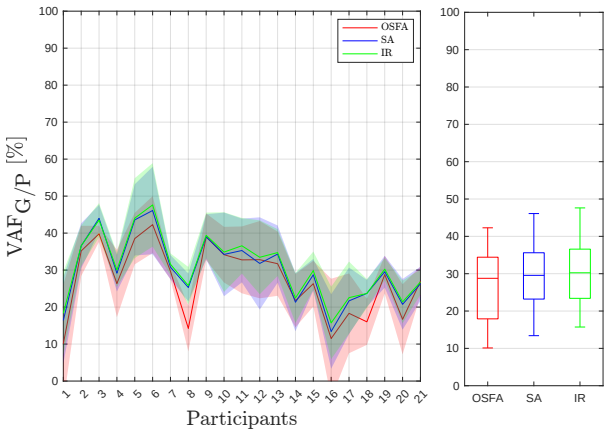

Fig. 20 Performance of the OSFA, SA and IR $H_{BDFT/G3}$ models for the identification of BDFT from the G3 data.

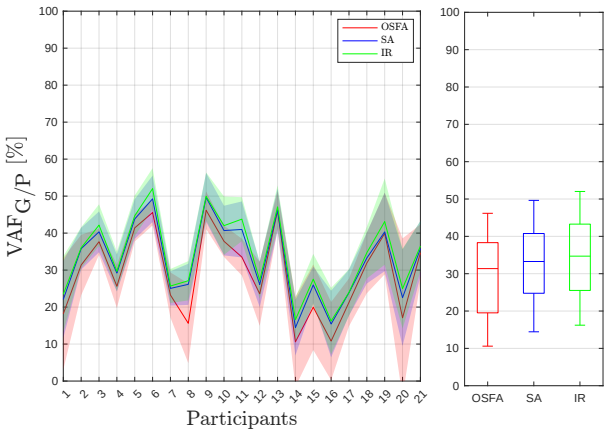

Fig. 21 Performance of the OSFA, SA and IR $H_{BDFT/M3}$ models for the identification of BDFT from the M3 data.

As already seen for the identification of the BDFT occurring with multisine disturbances, the more a BDFT model is tailored to the data, the better the performance. With the OSFA model, a median $VAF_{G/P}$ of 28.8% is reached, a number that increases to 29.6% for the SA model and to 30.2% for the IR model. The differences in identification performance across the models were proven to be highly significant with a Friedman's test and with post-hoc Wilcoxon signed-rank tests ($p < 0.01$).

To verify whether the accuracy of the identification of the Gaussian model $H_{BDFT/G3}$ is comparable to the identification of the $H_{BDFT/M3}$ model for the multisine signal, the performance of the $H_{BDFT/M3}$ model is shown in Fig. 21. Here the same $VAF_{G/P}$ from Eq. (9) is calculated for the M3 data, in contrast to the multisine-tailored VAF_M in Eq. (8) that was previously shown in Fig. 11. With the OSFA model identified for the multisine motion disturbance, the $VAF_{G/P}$ index indicates only 31.4% performance, 49% less than indicated by the more accurate multisine specific VAF_M in Eq. (8). Similarly, with the SA model a performance of 33.3% is noted (53.8% less than measured with the multisine specific VAF_M), 34.7% with the IR model (55.7% less). These numbers suggest that there is an approximately -50% offset in the performance measured using the generic $VAF_{G/P}$ index, which is caused by the contribution of the remnant over the frequency spectrum. Recalling the definition of the generic $VAF_{G/P}$ in Eq. (9), this contribution was estimated using the TSC inputs recorded in the NM condition. This estimate can never be fully accurate, as the realization of the TSC input signal is never the same across repeated runs. In conclusion, accounting for this bias, BDFT modeling with the G3 conditions achieves a performance that is comparable to the multisine case when using the OSFA and SA models (Wilcoxon signed-rank tests, $p \geq 0.05$, differences not significant). Only with the IR model, significantly less accurate models are found for the Gaussian turbulence BDFT (Wilcoxon signed-rank tests, $0.01 \leq p < 0.05$).

The differences in the BDFT dynamics of the M3 and G3 conditions were evaluated using the median and spread across participants of the parameters of the $H_{BDFT/M3}$ and $H_{BDFT/G3}$ models, shown with a boxplot in Fig. 22. Compared to the multisine condition, the Gaussian condition shows 59% lower feedthrough gain G_{BDFT}, a 81% higher damping (ζ_{BDFT}), and a 20% higher break frequency ω_{BDFT}. It should be noted that the time delay τ_{BDFT} for model $H_{BDFT/G3}$ is assumed to be equal to the τ_{BDFT} values found for $H_{BDFT/M3}$.

Finally, the capability of the SA models for the cancellation of BDFT from the TSC input signal on the G3 condition were evaluated through a comparison of the performance attained with the $H_{BDFT/G3}(j\omega)$ models (Fig. 23) and the $H_{BDFT/M3}(j\omega)$ models, as shown in Fig. 24. For comparison, Fig. 24 also shows the cancellation performance of the $H_{BDFT/M3}(j\omega)$ model for the M3 dataset, calculated using the CI on the entire frequency spectrum, Eq. (10). Both figures also show the performance of the two models in canceling BDFT with the high-intensity Patchy turbulence motion condition P3 (green data); these results will, however, only be discussed in Section IV.D. Unlike previous cancellation performance results, the axis limits in these plots show that here both negative CI values (the BDFT component of the input signal being canceled) and positive CI values (disturbance related contributions are increasing rather than being canceled) were obtained.

On the G3 data, the $H_{BDFT/G3}(j\omega)$ models have a cancellation performance of -29.6% (median CI), greatly outperforming $H_{BDFT/M3}(j\omega)$ which effectively adds to the TSC input components linearly related to the disturbance

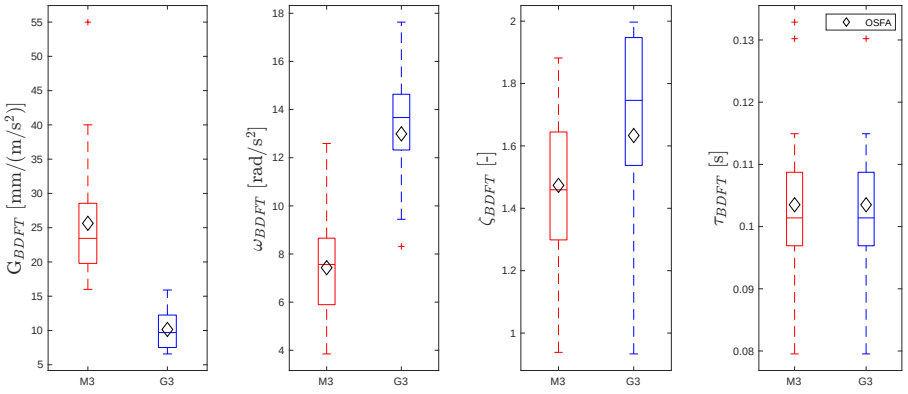

Fig. 22 Median and spread of the parameters of the model identified from high intensity Gaussian BDFT data $H_{BDFT/G3}$ and from high intensity multisine BDFT data $H_{BDFT/M3}$ (time domain approach, SA and OSFA model). The time delay τ_{BDFT} for model $H_{BDFT/G3}$ is fixed to the values found for model $H_{BDFT/M3}$.

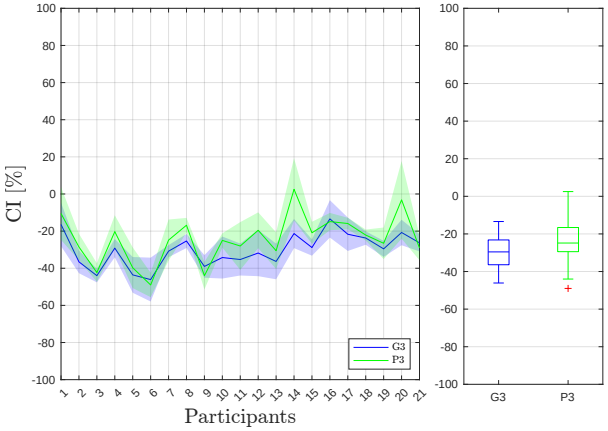

Fig. 23 Cancellation performance of model $H_{BDFT/G3}$ on BDFT occurring in G3 and P3 conditions (time domain approach, SA model, CI evaluated on the full frequency spectrum).

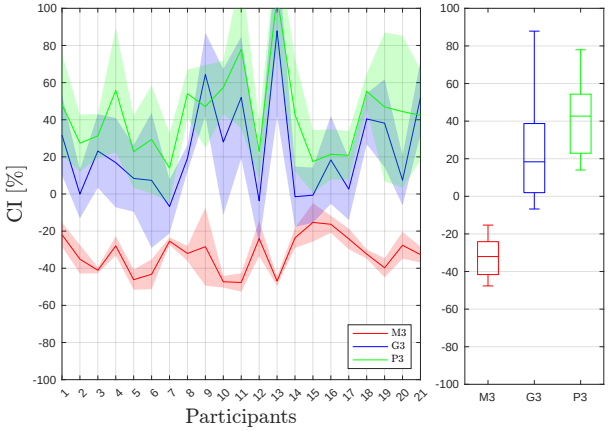

Fig. 24 Cancellation performance of model $H_{BDFT/M3}$ on BDFT occurring in M3, G3 and P3 conditions (time domain approach, SA model, CI evaluated on the full frequency spectrum).

rather than canceling them (median CI = 18.4%). As with the model identification performance, these results can only be compared to the multisine performance results when using the same performance index. For the M3 case, the median CI of the BDFT cancellation performance is -32.0%, only 2.5% better than Gaussian cancellation with the $H_{BDFT/G3}(j\omega)$ models; a difference that proved to be non-significant (Wilcoxon signed-rank test, $p \geq 0.05$). In conclusion, model-based BDFT mitigation works almost as well in steady-state realistic turbulence (G3) as with a multisine motion disturbance (M3). Still, since the BDFT dynamics are different in both cases, identification of a dedicated BDFT model in realistic turbulent conditions is required.

D. Biodynamic Feedthrough Mitigation in Patchy Turbulence

The effect of turbulence variability on performance of model-based BDFT mitigation was analyzed using the Patchy turbulence condition P3. In particular, this research set out to quantify how much the variability in the motion disturbance may affect performance of time-invariant BDFT models as identified from time-invariant turbulence (G3 or M3). Hence, the cancellation performance of the patchy turbulence is shown in Fig. 23 and 24, respectively, for the $H_{BDFT/G3}(j\omega)$ and $H_{BDFT/M3}(j\omega)$ SA models. The model identified from the multisine motion disturbance data fails to cancel BDFT (median CI = 42.7%), resulting in amplified BDFT as also seen with the cancellation in Gaussian turbulence in Fig. 24. However, the BDFT models identified from the Gaussian turbulence data effectively cancel the P3 BDFT with a performance of CI = -24.8%; this is 4.7% lower than the performance of this model in non-varying

Gaussian turbulence, and 7.2% lower compared to cancellation of BDFT in the multisine motion disturbance. These differences were shown to be highly significant with Friedman's test and post-hoc Wilcoxon signed-rank tests ($p < 0.01$).

To infer the causes of these differences, the modeling error as a function of time was calculated for the G3 and P3 cases using Eq. (12). The average of the modeling error, calculated across the experimental runs for the two conditions and across participants, is plotted as a function of time in Fig. 25 for a interval of 40 seconds, below the corresponding disturbance signals. As the motion disturbance signal was always the same in all runs performed with a specific motion signal (M3, G3, P3), the modeling errors can be validly averaged.

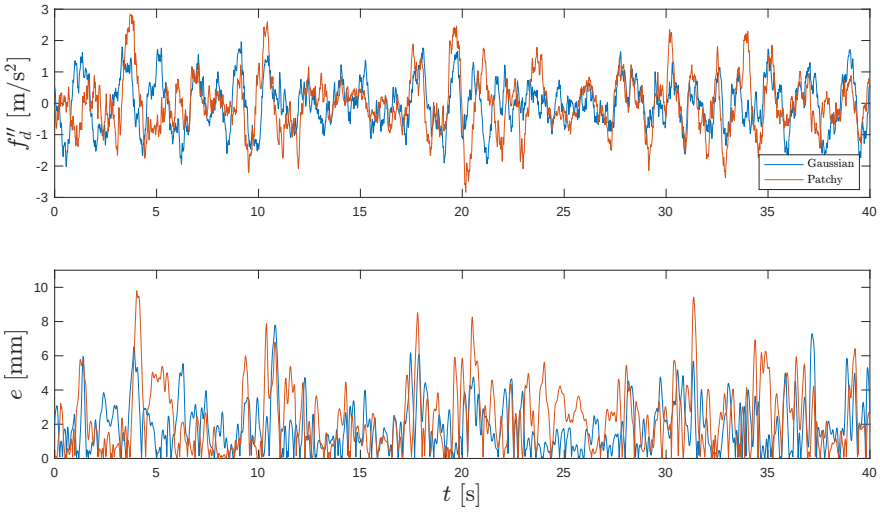

Fig. 25 Comparison between Gaussian and patchy motion disturbances and the absolute value of the error between measured and modeled BDFT component of the TSC input for the two disturbances, averaged across participants (SA model, $H_{BDFT/G3}$).

The P3 motion disturbance (top panel of Fig. 25 in red) frequently shows peaks with high accelerations (for example at 3, 10, 20 seconds) and a higher magnitude than the peaks visible in the Gaussian motion disturbance. From the bottom panel of Fig. 25, it can be seen that the modeling error indeed seems to be higher in correspondence to these peaks, especially when accelerations are steep (for example at 3 and 20 seconds). Given these findings, it seems likely that the variability present in the patchy turbulence is indeed the primary cause for the small, yet significant, difference in BDFT cancellation performance for the patchy turbulence case. It should be noted, however, that mitigation performance for the Gaussian case is being evaluated directly on the identification dataset, in contrast to the patchy turbulence being a separate evaluation dataset, and that this could affect the magnitude of the difference in cancellation performance between the two cases.

E. Biodynamic Feedthrough Mitigation in Gaussian and Patchy Turbulence at Low and Medium Intensities

Analysis of the BDFT induced by the G2, G1, P2, and P1 motion disturbances were consistent with the findings discussed in previous sections. The models identified from the low- and medium-intensity multisine motion disturbances ($H_{BDFT/M1}(j\omega)$ and $H_{BDFT/M2}(j\omega)$) are outperformed by models identified with Gaussian turbulence ($H_{BDFT/G1}(j\omega)$ and $H_{BDFT/G2}(j\omega)$) for all IR, SA and OSFA models. As also found when comparing the BDFT models for different intensities of the multisine disturbance in Section IV.B, BDFT identification results become less accurate when intensity decreases; on average, in comparison to $H_{BDFT/G3}(j\omega)$, a performance decrease of -5.8% is seen for $H_{BDFT/G2}(j\omega)$, -12.5% for $H_{BDFT/G1}(j\omega)$. Consequently, cancellation performance also decreases with decreasing intensity. In fact, the median value of CI is on average -21.6% for the medium intensity and -14.2% for the low intensity, with cancellation of BDFT for the Gaussian conditions outperforming cancellation for the Patchy conditions by 3.3% and 4.7%, respectively, at medium and low intensity. Again, this suggests that turbulence variability may need to be accounted for in BDFT mitigation. Fig. 26 gives the median and spread of the parameters of the Gaussian BDFT models fitted for all intensities. As done for the identification of $H_{BDFT/G3}(j\omega)$, for $H_{BDFT/G2}(j\omega)$ and $H_{BDFT/G1}(j\omega)$ the time delay τ_{BDFT} was kept fixed to the identified values for M2 and M1, respectively.

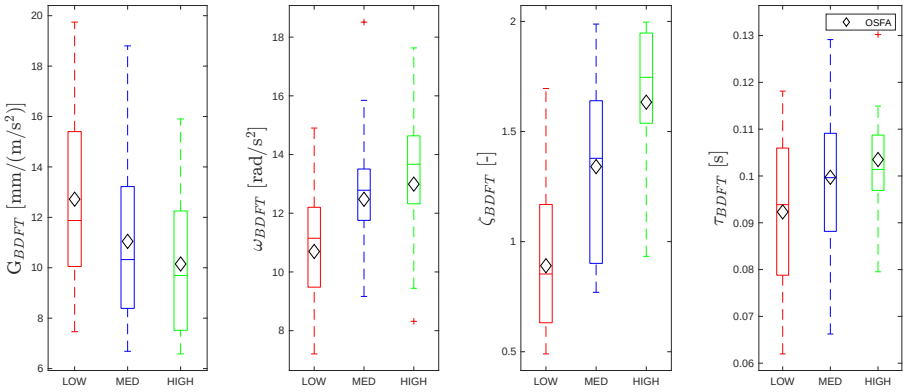

Fig. 26 Median and spread of the parameters of the $H_{BDFT/G}(j\omega)$ models across intensities (time domain approach, SA and OSFA models).

Compared to the trends seen in the parameters of the multisine models in Fig. 16, clear differences are seen in the gain values G_{BDFT} and break frequencies ω_{BDFT} across intensities for the Gaussian turbulence; as motion intensity decreases the values of the gain increase and those of the break frequency decrease. On average, a 51% lower gain and a 79% higher break frequency are seen in Gaussian models $H_{BDFT/G}(j\omega)$ compared to multisine models $H_{BDFT/M}(j\omega)$. These findings confirm that differences between multisine and Gaussian motion disturbance persist also at medium and low intensity and hence would also need to be accounted for in BDFT mitigation.

V. Discussion

In this paper, a human-in-the-loop flight simulator experiment was used to evaluate the effect of turbulence variability and intensity on the biodynamic feedthrough (BDFT) occurring in touchscreen (TSC) dragging tasks. The ultimate objective of this research is to develop model-based BDFT mitigation techniques that may improve the use of TSC interfaces in aircraft cockpits. The study, performed on the SIMONA Research Simulator (SRS) at TU Delft, involved 21 participants performing a tracking task on a TSC placed directly in front of them. Three types of motion disturbance were tested: a multisine disturbance resembling aircraft accelerations caused by turbulence, and two simulated realistic aircraft turbulence responses, differing in their variability (invariant perceived Gaussian turbulence and variable Patchy turbulence). All these conditions were tested at three levels of motion intensity, together with a reference static condition.

Unlike hypothesized (**H1**), significantly less than 90% of the BDFT component of the input was successfully modeled by personalized (subject-average) BDFT models at the high intensity multisine condition. The current experiment achieved a 5.6% lower identification quality-of-fit compared to the earlier experiment of [13], despite the use of the same exact same forcing function and experimental set-up. Hence, Hypothesis 1 is rejected. A link was found between identification performance and variability in BDFT measured across experimental runs, with low model performance being correlated to high intra-subject variability. This increased variability seen in participants of this research compared to [13] was, in hindsight, most likely caused by increased fatigue and boredom due to the longer duration of the experiment and the increased amount of conditions to which participants were exposed.

With **H2**, it was hypothesized that high motion intensity BDFT would be larger in magnitude compared to medium and low motion intensity, and that therefore high-intensity BDFT models would not be suitable for mitigation at medium and low intensities. This part of the hypothesis was evaluated using only the multisine motion disturbance conditions. A second statement hypothesized that the success of model-based BDFT mitigation would be independent of the motion intensity if applied using a model identified for the same motion intensity at which cancellation is being employed. In relation to the first part of **H2**, the generalizability of a BDFT model across intensities was evaluated for both the Subject-Averaged (SA) and One-Size-Fits-All (OSFA) models. For the SA models, it was shown that the M3 and M2 models present an equivalent match with the M2 data, canceling over 84% of the BDFT component of the input. However, when applied on M1 data, the M3 model gives a 4.3% lower performance compared to the M1 model. This is due to a 49% decrease in damping ratio visible in the identification of the M1 data compared to the M3 data. For the OSFA models, the model identified from M3 data was shown to perform comparably for cancellation on M2 and M1 data, although achieving on average 6.5% lower performance compared to the SA models. The first statement in **H2** is

therefore partially disproven, as no SA models can be truly generalized across intensities, while OSFA models can be, though at the cost of a loss of overall accuracy.

For the second statement of **H2**, it was shown that performance of the model-based BDFT mitigation is influenced by the intensity of the accelerations causing BDFT, disproving this part of the hypothesis. In particular the mitigation at lower intensities was shown to achieve a lower performance compared to mitigation at higher intensities (canceling 86.8%, 84.2% and 69.7% of the BDFT component of the input for M3, M2 and M1, respectively). The reason for this was found through an analysis of the non-linearities in the TSC input at the frequencies of the disturbance signal. Increasingly reduced signal-to-noise ratios were found in the signals registered from medium and low motion intensity, especially at low frequencies, due to a lower amount of feedthrough present in the TSC input. The same decrease in mitigation performance with decreasing intensity was further confirmed with the BDFT occurring with the Gaussian and Patchy turbulence.

The study of the dynamics of BDFT in Gaussian turbulence revealed considerable differences with the dynamics of BDFT occurring with the multisine motion disturbance. Overall, the results oppose the first statement of **H3**, which postulated more compliant neuromuscular dynamics in Gaussian turbulence, as an increase in stiffness and damping was noted for G3 compared to M3, as well as a decrease in the magnitude of BDFT. The same differences were also observed at medium and low intensities. The first part of **H3** is therefore rejected. It follows that a BDFT model identified with the used multisine signal was unable to mitigate BDFT occurring in realistic Gaussian turbulence. Using a time-domain estimator to better match the BDFT models with the Gaussian high-intensity turbulence, SA BDFT models were shown to still effectively cancel the occurring BDFT, with comparable performance to mitigation in the multisine motion disturbance case.

Evaluating a cancellation index over the full frequency spectrum, a performance of 29.6% was achieved by SA models in Gaussian conditions in comparison to 32.0% for the multisine case. It should, however, be noted that the evaluation of the performance for the Gaussian case is subject to a bias leading to higher evaluation performance, due to the lack of two separate datasets for identification of the model and evaluation of the BDFT performance. With this, the second part of **H3**, hypothesizing that model-based BDFT mitigation in realistic turbulence conditions would be effective when adapting the model parameters, is accepted. Equivalent conclusions were drawn from the medium and low turbulence intensity BDFT data.

Finally, **H4** postulated that BDFT cancellation for the Patchy turbulence with a time-invariant BDFT model would result in lower performance due to the variability of the turbulence over time. It was found that the model identified in the high intensity Gaussian turbulence condition (G3) is in fact able to effectively cancel BDFT also for the corresponding Patchy turbulence condition (P3), although with a 4.7% lower performance. Comparison of the timing of peaks in the BDFT modeling error with the occurrence of steep accelerations in the P3 condition suggested that the time-varying turbulence intensity variations indeed seem to correlate with modeling error magnitude. Similarly using the medium and low intensity data, Gaussian models were shown to effectively cancel BDFT for the Patchy turbulence, although with lower performance compared to the cancellation of BDFT in Gaussian turbulence. **H4** is therefore accepted.

To conclude this discussion, a few comments are left for future work. From the results of this experiment, several factors causing changes in the dynamics of BDFT were highlighted. Among these, fatigue, turbulence spectrum, turbulence intensity, and the type of control task performed on the TSC are the most pressing. For the first point, it is strongly recommended to limit the duration (and number of conditions) for future BDFT experiments. Especially experiments that focus on TSC operation with a screen mounted vertically in front of participants, requiring an extended arm for TSC interaction, can be quite physically demanding. Hence, better data consistency is likely obtained with shorter, focused, experiments. A second crucial recommendation is to verify the correspondence between the BDFT dynamics that participants show with multisine and Gaussian turbulence spectra for a case where they were more deliberately matched. The multisine disturbance signal used in the current experiment was taken from earlier experiments [13, 14] and hence not as accurately matched with the spectrum of the realistic Gaussian turbulence as is possible with a multisine, see e.g. [30].

In the current experiment, also considerable variations in the BDFT model's gain, break frequency and damping ratio were observed across the tested turbulence intensities. As a consequence, no generalized model achieves a consistently high performance in mitigating BDFT for the measured TSC control inputs. Instead, Individual Run (IR) models were shown to consistently achieve higher performance for all types of motion tested and the different motion intensities, as long as enough feedthrough is occurring. This leads to the conclusion that real-time adaptation of the parameters of the BDFT model may be needed in practice. This would require time-varying estimation methods and time-varying BDFT models, using techniques such as the dual extended Kalman filter method [31] or recursive autoregressive exogenous model structures identified in real-time [32, 33]. Findings highlighting a connection between turbulence variability

and increased BDFT modeling errors for the Patchy turbulence case also suggest that time-varying BDFT models and estimation techniques would outperform the currently used time-invariant methods. Future work should replicate the experiment to explicitly quantify how much can be gained in terms of mitigation performance with time-varying methods.

Finally, previous research has shown that also the control task performed on the TSC can greatly influence the occurring BDFT [13–15]. The control task used to collect BDFT data in the current experiment was designed with the purpose of facilitating the identification of BDFT, and as such lacks the realism when compared to possible tasks performed by pilots in real aircraft cockpits. Furthermore, in the current experiment participants wore anti-static gloves to reduce fatigue and wear due to friction in the prolonged contact of the participants' finger with the TSC. As the reduced friction experienced with anti-static gloves also may affect BDFT susceptibility, and as a result how TSC users adapt their neuromuscular stiffness to counter BDFT, performing experiments with different tasks and with forced variations in TSC-finger friction level will enable the further verification of the applicability of model-based BDFT mitigation in aircraft cockpits.

A final comment should be made on the applicability of the findings of this experiment in real flight. The stationary (Gaussian) turbulence and the variable (patchy) turbulence conditions tested were not a fully accurate simulation of aircraft vertical accelerations caused by turbulence, but rather a filtered version of these, designed to be simulated within the motion space of the SIMONA Research Simulator. The effects of these filters, a low-pass filter and a classical high-pass washout filter, can only be fully taken out of the equation by replicating the experiment in actual aircraft cockpits and real flight. In consideration to this and other points made in this discussion, it is hereby emphasized that such an experiment is required for the ultimate assessment of the impact of turbulence and turbulence variability on BDFT.

VI. Conclusions

This paper explored the impact of turbulence on model-based biodynamic feedthrough (BDFT) mitigation for touchscreen (TSC) dragging tasks, which would enable canceling on a software level the involuntary inputs due to aircraft motion perturbations (e.g., turbulence). In particular, the effects of turbulence acceleration variability and intensity were explored through a human-in-the-loop moving-base simulator experiment. Three different heave motion disturbances were simulated: a multisine motion disturbance from previous work, a realistic turbulent flight condition perceived as time invariant in the cockpit (Gaussian condition), and a time-varying turbulent flight condition (Patchy condition), each at three different motion intensities. Using the high intensity multisine motion disturbance it was shown that personalized (subject-average) BDFT models can be used to cancel over 80% of the involuntary components of the input, over 90% with models identified on an individual measurement. Overall, both variations in BDFT in time (due to turbulence variations) and across participants were found to have a significant impact on BDFT modeling and mitigation. Hence, highly personalized models seem preferable for achieving the most promising BDFT cancellation results. Testing model-based BDFT mitigation at three levels of turbulence intensity, it was shown that with decreasing intensity the amount of BDFT in the TSC input decreases, which lowers the signal-to-noise ratio and makes the identified models less accurate. The damping ratio of the BDFT dynamics was shown to be affected most strongly by turbulence intensity variations, and decreased with decreasing intensity. Despite these variations, the high-intensity BDFT models were shown to mitigate around 84% of the BDFT component of the input both for the high- and medium-intensity data, while only about 65% for the low motion intensity. Mitigation with was tested on BDFT occurring in a simulated stationary (Gaussian) turbulence condition. For the realistic Gaussian turbulence, it was found that BDFT models identified with a multisine motion disturbance were unable to effectively cancel BDFT, and in some cases even enhanced the perturbation of the TSC input (positive cancellation index CI = 18.4%). However, using a time-domain parameter estimation technique it was possible to explicitly match the BDFT model with the BDFT induced by the Gaussian turbulence, so that again effective BDFT mitigation can be achieved (CI = -29.6%, only 2.4% worse than obtained for the multisine data). Finally, for the Patchy turbulence with variable characteristics, effective BDFT mitigation performance was still achieved using the model identified for Gaussian turbulence (CI = -24.8%, 4.7% lower when compared to Gaussian turbulence). The variability present in the Patchy turbulence was also found to correlate with the BDFT modeling error, emphasizing that future work should focus on time-varying BDFT models and real-time identification of parameters to further improve BDFT mitigation performance.

References

[1] Degani, A., Palmer, E. A., and Bauersfeld, K. G., ""Soft" controls for hard displays: Still a challenge," *Proceedings of the Human Factors Society Annual Meeting*, Vol. 36, SAGE Publications Sage CA: Los Angeles, CA, 1992, pp. 52–56. https://doi.org/10.1177/154193129203600114.

[2] Hutchins, E. L., Hollan, J. D., and Norman, D. A., "Direct manipulation interfaces," *Human–computer interaction*, Vol. 1, No. 4, 1985, pp. 311–338. https://doi.org/10.1201/b15703-5.

[3] Dodd, S. R., Lancaster, J., Grothe, S., DeMers, B., Rogers, B., and Miranda, A., "Touch on the flight deck: The impact of display location, size, touch technology & turbulence on pilot performance," *2014 IEEE/AIAA 33rd Digital Avionics Systems Conference (DASC)*, IEEE, 2014, pp. 2C3–1. https://doi.org/10.1109/dasc.2014.6979570.

[4] Rouwhorst, W., Verhoeven, R., Suijkerbuijk, M., Bos, T., Maij, A., Vermaat, M., and Arents, R., "Use of touch screen display applications for aircraft flight control," *2017 IEEE/AIAA 36th Digital Avionics Systems Conference (DASC)*, IEEE, 2017, pp. 1–10. https://doi.org/10.1109/dasc.2017.8102060.

[5] Van Zon, N. C. M., Borst, C., Pool, D. M., and Van Paassen, M. M., "Touchscreens for Aircraft Navigation Tasks: Comparing Accuracy and Throughput of Three Flight Deck Interfaces Using Fitts' Law," *Human Factors: The Journal of the Human Factors and Ergonomics Society*, Vol. 62, 2019. https://doi.org/10.1177/0018720819862146.

[6] Coutts, L. V., Plant, K. L., Smith, M., Bolton, L., Parnell, K. J., Arnold, J., and Stanton, N. A., "Future technology on the flight deck: assessing the use of touchscreens in vibration environments," *Ergonomics*, Vol. 62, No. 2, 2019, pp. 286–304. https://doi.org/10.1080/00140139.2018.1552013.

[7] Kaminani, S., "Human computer interaction issues with touch screen interfaces in the flight deck," *2011 IEEE/AIAA 30th Digital Avionics Systems Conference*, IEEE, 2011, pp. 6B4–1. https://doi.org/10.1109/dasc.2011.6096098.

[8] Venrooij, J., Mulder, M., Van Paassen, M. M., Mulder, M., and Abbink, D. A., "A review of biodynamic feedthrough mitigation techniques," *IFAC Proceedings Volumes*, Vol. 43, No. 13, 2010, pp. 316–321. https://doi.org/10.3182/20100831-4-fr-2021.00056.

[9] Tao, D., Zeng, J., Liu, K., and Qu, X., "Effects of control-to-display gain and operation precision requirement on touchscreen operations in vibration environments," *Applied Ergonomics*, Vol. 91, 2021, p. 103293. https://doi.org/10.1016/j.apergo.2020.103293.

[10] Cockburn, A., Gutwin, C., Palanque, P., Deleris, Y., Trask, C., Coveney, A., Yung, M., and MacLean, K., "Turbulent touch: Touchscreen input for cockpit flight displays," *International Conference for Human-Computer Interaction (CHI 2017)*, 2017, pp. 6742–6753. https://doi.org/10.1145/3025453.3025584.

[11] Cockburn, A., Masson, D., Gutwin, C., Palanque, P., Goguey, A., Yung, M., Gris, C., and Trask, C., "Design and evaluation of braced touch for touchscreen input stabilisation," *International Journal of Human-Computer Studies*, Vol. 122, 2019, pp. 21–37. https://doi.org/10.1016/j.ijhcs.2018.08.005.

[12] Lancaster, J., De Mers, B., Rogers, B., Smart, A., and Whitlow, S., "57.3: The Effect of Touch Screen Hand Stability Method on Performance & Subjective Preference in Turbulence," *SID Symposium Digest of Technical Papers*, Vol. 42, Wiley Online Library, 2011, pp. 841–844. https://doi.org/10.1889/1.3621464.

[13] Khoshnewiszadeh, A., and Pool, D. M., "Mitigation of Biodynamic Feedthrough for Touchscreens on the Flight Deck," *International Journal of Human–Computer Interaction*, 2021, pp. 1–13. https://doi.org/10.1080/10447318.2021.1890490.

[14] Mobertz, X., Pool, D. M., van Paassen, M., and Mulder, M., "A Cybernetic Analysis of Biodynamic Effects in Touchscreen Operation in Turbulence," *2018 AIAA Modeling and Simulation Technologies Conference*, 2018. https://doi.org/10.2514/6.2018-0115.

[15] Pool, D. M., and Vardar, Y., "FITS: Ensuring Safe and Effective Touchscreen Use in Moving Vehicles," *Proceedings of the 5th IFAC Workshop on Cyber-Physical and Human Systems, Antalya, Turkey*, 2024.

[16] Alapetite, A., Fogh, R., Zammit-Mangion, D., Zammit, C., Agius, I., Fabbri, M., Pregnolato, M., and Becouarn, L., "Direct tactile manipulation of the flight plan in a modern aircraft cockpit," *Proc. of HCI Aero*, 2012. URL https://www.researchgate.net/profile/Alexandre-Alapetite/publication/260297675_Direct_tactile_manipulation_of_the_flight_plan_in_a_modern_aircraft_cockpit/links/00b7d530b16b6dc72e000000/Direct-tactile-manipulation-of-the-flight-plan-in-a-modern-aircraft-cockpit.pdf.

[17] Smith, M. A., Plant, K. L., Parnell, K. J., Wynne, R. A., and Stanton, N. A., "P-28: Investigating the Usability of Touchscreen Interfaces in a Turbulent Flight Deck–For Panning and Numeric Data Entry Tasks," *SID Symposium Digest of Technical Papers*, Vol. 51, Wiley Online Library, 2020, pp. 1438–1441. https://doi.org/10.1002/sdtp.14158.

[18] Abrahamsson, H., and Karlsson, L., "Case Study: Digitization of a User Interface: Investigating the use of a touch screen in Helicopter 14," , 2020. https://doi.org/urn:nbn:se:kth:diva-276838.

[19] Zaal, P. M. T., Pool, D. M., Chu, Q. P., Van Paassen, M. M., Mulder, M., and Mulder, J. A., "Modeling human multimodal perception and control using genetic maximum likelihood estimation," *Journal of Guidance, Control, and Dynamics*, Vol. 32, No. 4, 2009, pp. 1089–1099. https://doi.org/10.2514/1.42843.

[20] McRuer, D., and Weir, D. H., "Theory of manual vehicular control," *Ergonomics*, Vol. 12, No. 4, 1969, pp. 599–633. https://doi.org/10.1080/00140136908931082.

[21] Mulder, M., Pool, D. M., Abbink, D. A., Boer, E. R., Zaal, P. M. T., Drop, F. M., van der El, K., and van Paassen, M. M., "Manual control cybernetics: State-of-the-art and current trends," *IEEE Transactions on Human-Machine Systems*, Vol. 48, No. 5, 2017, pp. 468–485. https://doi.org/10.1109/thms.2017.2761342.

[22] Vrouwenvelder, S., Postema, F., and Pool, D. M., "Measuring the Drag Latency of Touchscreen Displays for Human-in-the-Loop Simulator Experiments," *AIAA Scitech 2021 Forum*, 2021. https://doi.org/10.2514/6.2021-0896.

[23] Leto, G., "Effect of Turbulence Intensity and Variability on Model-Based Biodynamic Feedthrough Mitigation with Touchscreen Dragging Tasks. Preliminary Report." Master's thesis, Unpublished. Delft University of Technology, 2023. URL https://resolver.tudelft.nl/uuid:287c7efb-d15d-4360-a785-c7441746b3f4.

[24] Jacobson, B., "A novel Fitts' law: Evaluating touch-based interfaces in atmospheric turbulence," Master's thesis, Unpublished. Delft University of Technology, 2021. URL http://resolver.tudelft.nl/uuid:2404d466-fbc9-4cca-ba54-097413df9eea.

[25] Van de Moesdijk, G. A. J., "The description of patchy atmospheric turbulence, based on a non-Gaussian simulation technique," *Delft University of Technology, Department of Aeronautical Engineering, Report VTH-192*, 1975. URL http://resolver.tudelft.nl/uuid:d9060267-cef5-4955-982a-1a7b5da25d90.

[26] Van de Moesdijk, G. A. J., "Non-Gaussian structure of the simulated turbulent environment in piloted flight simulation," *Technische Hogeschool Delft, Vliegtuigbouwkunde, memorandum m-304*, 1978. URL http://resolver.tudelft.nl/uuid:b5e66aad-6a6e-44e8-af4d-58d51684c515.

[27] Mulder, J. A., van der Vaart, J. C., van Staveren, W. H. J. J., Chu, Q. P., and Mulder, M., *Aircraft Responses to Atmospheric Turbulence: Lecture Notes AE4304*, TU Delft, 2016.

[28] Van Der Linden, C. A. A. M., "DASMAT-Delft University aircraft simulation model and analysis tool: A Matlab/Simulink environment for flight dynamics and control analysis," *Series 03: Control and Simulation 03*, 1998.

[29] Gouverneur, B., Mulder, J. A., van Paassen, M. M. R., Stroosma, O., and Field, E., "Optimisation of the SIMONA Research Simulator's Motion Filter Settings for Handling Qualities Experiments," *AIAA Modeling and Simulation Technologies Conference and Exhibit*, American Institute of Aeronautics and Astronautics, 2003, p. 5679. https://doi.org/10.2514/6.2003-5679.

[30] Kolff, M. J. C., Van der El, K., Pool, D. M., Van Paassen, M. M., and Mulder, M., "Approximating Road Geometry with Multisine Signals for Driver Identification," *IFAC-PapersOnline*, Vol. 52, No. 19, 2019, pp. 341–346. https://doi.org/10.1016/j.ifacol.2019.12.082.

[31] Popovici, A., Zaal, P., and Pool, D. M., "Dual extended Kalman filter for the identification of time-varying human manual control behavior," *AIAA Modeling and Simulation Technologies Conference*, 2017, p. 3666.

[32] Van Grootheest, A., Pool, D. M., van Paassen, M., and Mulder, M., "Identification of Time-Varying Manual Control Adaptations with Recursive ARX Models," *2018 AIAA Modeling and Simulation Technologies Conference*, 2018, p. 0118.

[33] Plaetinck, W., Pool, D., van Paassen, M., and Mulder, M., "Online identification of pilot adaptation to sudden degradations in vehicle stability," *IFAC-PapersOnLine*, Vol. 51, No. 34, 2019, pp. 347–352.